

Revealing the Chemical Structure of the Magellanic Clouds with APOGEE. I. Calculating Individual Stellar Ages of RGB Stars in the Large Magellanic Cloud

Joshua T. Povick¹*, David L. Nidever¹, Pol Massana¹, Jamie Tayar^{2,3}, Knut A.G. Olsen⁴, Sten Hasselquist^{5,6}, Maria-Rosa L. Cioni⁷, Christian Nitschelm⁸, Ricardo Carrera⁹, Yumi Choi^{4,10}, Alexandre Roman-Lopes¹¹, Steven R. Majewski¹², Andrés Almeida¹², Katia Cunha^{13,14,15} and Verne V. Smith⁴

¹Department of Physics, Montana State University, P.O. Box 173840, Bozeman, MT 59717-3840

²Department of Astronomy, University of Florida, Bryant Space Science Center, Stadium Road, Gainesville, FL 32611, USA

³Institute for Astronomy, University of Hawai‘i at Mānoa, 2680 Woodlawn Drive, Honolulu, HI 96822, USA

⁴NSF’s National Optical-Infrared Astronomy Research Laboratory, 950 N. Cherry Ave., Tucson, AZ 85719, USA

⁵Department of Physics & Astronomy, University of Utah, Salt Lake City, UT 84112, USA

⁶Space Telescope Science Institute, 3700 San Martin Drive, Baltimore, MD 21218

⁷Leibniz-Institut für Astrophysik Potsdam, An der Sternwarte 16, D-14482 Potsdam, Germany

⁸Centro de Astronomía (CITEVA), Universidad de Antofagasta, Avenida Angamos 601, Antofagasta 1270300, Chile

⁹INAF-Osservatorio di Astrofisica e Scienza dello Spazio di Bologna, via P. Gobetti 93/3, 40129, Bologna, Italy

¹⁰Department of Astronomy, University of California Berkeley, Berkeley, CA 94720, USA

¹¹Departamento de Astronomía, Facultad de Ciencias, Universidad de La Serena, Av. Juan Cisternas 1200, La Serena, Chile

¹²Department of Astronomy, University of Virginia, Charlottesville, VA 22904-4325, USA

¹³Steward Observatory, University of Arizona, 933 North Cherry Avenue, Tucson, AZ, 85721, USA

¹⁴Observatório Nacional, Rua General José Cristino, 77, 20921-400 São Cristóvão, Rio de Janeiro, RJ, Brazil

¹⁵Institut d’Astrophysique de Paris, UMR 7095 CNRS, Sorbonne Université, 98bis Bd. Arago, 75014 Paris, France

Accepted XXX. Received YYY; in original form ZZZ

ABSTRACT

Stellar ages are critical for understanding the temporal evolution of a galaxy. We calculate the ages of over 6000 red giant branch stars in the Large Magellanic Cloud (LMC) observed with SDSS-IV / APOGEE-S. Ages are derived using multi-band photometry, spectroscopic parameters (T_{eff} , $\log g$, $[\text{Fe}/\text{H}]$, and $[\alpha/\text{Fe}]$) and stellar isochrones and the assumption that the stars lie in a thin inclined plane to get accurate distances. The isochrone age and extinction are varied until a best match is found for the observed photometry. We perform validation using the APOKASC sample, which has asteroseismic masses and accurate ages, and find that our uncertainties are $\sim 20\%$ and range from $\sim 1\text{--}3$ Gyr for the calculated age values. Here we present the LMC age map as well as the age-radius relation and an accurate age-metallicity relation (AMR). The age map and age-radius relation reveal that recent star formation in the galaxy was more centrally located and that there is a slight dichotomy between the north and south with the northern fields being slightly younger. The northern fields that cover a known spiral arm have median ages of ≥ 2 Gyr, which is the time when an interaction with the SMC is suggested to have happened. The AMR is mostly flat especially for older ages although recently (about 2.0–2.5 Gyr ago) there is an increase in the median $[\text{Fe}/\text{H}]$. Based on the time frame, this might also be attributed to the close interaction between the LMC and SMC.

Key words: techniques: miscellaneous – galaxies: evolution – stars: evolution – galaxies: dwarf – Magellanic Clouds

1 INTRODUCTION

The ages of stars is very important for understanding galaxy evolution and galactic archaeology. Without temporal information it becomes much more difficult to pinpoint how galaxies evolved to what we see today. Unfortunately, determining ages is not without its challenges as we rely on indirect means to find ages. Often times limited photometry or low resolution spectra make ages nearly impossible to

determine because there is not enough information to constrain the ages of stars provided by these methods.

Stellar clusters have been accurately age-dated for many decades, taking advantage of the age-sensitivity of turnoff and subgiant branch stars (e.g. Sandage 1970; Flower et al. 1983; Sarajedini 2008). It is substantially more challenging to measure the ages of individual field stars. However, there are several methods that have been developed to calculate ages of individual stars. Some of the more popular methods include: nucleocosmochronometry, gyrochronology, asteroseismology, chemical abundance ratios, and using isochrones. Nucleocos-

* E-mail: joshua.povick@montana.edu

mochronometry relies on measuring the abundance of radioactive nuclides and their daughter products and is much like the analog of radiocarbon dating, but for stars (Hill et al. 2002; Frebel et al. 2007). Very high signal-to-noise and high resolution spectra are required to make these measurements and even then the relevant absorption lines may not exist in the spectrum. In general, nucleocosmochronometry has only been performed for a small number of stars. Gyrochronology uses the rotation rate of a star to calculate its age because as a star ages its rotational speed decreases (Barnes 2007; Mamajek & Hillenbrand 2008). This requires precise, time-series photometry of cool, main-sequence stars which can be challenging to obtain for external galaxies like the LMC. Asteroseismology uses scaling relations and the oscillations inside of a star to obtain precise masses and then ages using isochrones (Cunha et al. 2007; Pinsonneault et al. 2014). Since mass and age are strongly anticorrelated on the giant branch, measuring mass accurately also allows for an accurate age to be determined. However, very precise and high-cadence photometry is required to derive good asteroseismologic masses and this is currently only available for small portions of the sky (i.e., Kepler, K2, CoRoT, TESS). More recently, spectroscopic chemical abundances have been used to determine masses of RGB stars with $[C/N]$ and $[C^{12}/C^{13}]$ ratios (Ness et al. 2016). These ratios are sensitive to the mass-dependent dredge-up that happens on the giant branch and pulls up nuclear-processed material from the interior. Currently, this technique only works for metal-rich populations ($[Fe/H] \gtrsim -0.5$), and, therefore, is not applicable for the relatively metal-poor LMC stars. Arguably one of the most popular methods to find ages is using isochrones. Isochrone-fitting involves fitting theoretical stellar models to either individual or groups of stars. Many of these methods rely on comparing to stellar evolutionary models and to be able to truly do this we need many photometric bands that constrain the spectral energy distribution (SED) or high resolution spectra. The BEAST (Gordon et al. 2016) compares a grid of isochrones to multi-band photometry to determine mass, age, metallicity, T_{eff} , and $\log g$ on a star-by-star basis. This has been used successfully in M31 using the PHAT survey (Dalcanton et al. 2012). All of these methods come with their own set of pros and cons and the choice of which one to use is often dictated by context.

Previous work of finding ages using isochrones for giant stars include works such as Feuillet et al. (2016). In that work ages are found two different ways: 1) calculating the mass from measured stellar parameters from which the mass–age relation can be used to get age and 2) using a Bayesian isochrone matching technique with a constant star formation history (SFH) to derive an age probability distribution for each star. Through mock data tests it was found that this method shows that decent ages can be derived for individual stars using a combination of photometry and spectroscopy with isochrones using a probabilistic approach.

This work uses isochrones to determine the age of individual red giant branch (RGB) stars using photometric and spectroscopic observations through direct calculation that is non-probabilistic. We take advantage of the fact that the absolute magnitude of giant stars vary substantially with age for fixed T_{eff} , by as much as 0.8 magnitudes between 1 Gyr and 10 Gyr at an average LMC metallicity of $[Fe/H] = -0.5$. One potential drawback of using isochrones is the age-metallicity degeneracy of RGB stars, but we overcome this by using the metallicity measured with high-resolution spectroscopy.

The method presented in this work finds the age by calculating the model photometry age in six different passbands spanning both optical and infrared wavelengths using a single common trial and comparing to the observed photometry of a star. This method is

possible due to accurate distances, which are needed to constrain the absolute magnitude of a star.

There are two main reasons for studying the ages of red giant branch (RGB) stars in the LMC. The first reason is that the literature is scant on the spatial distribution of ages in the galaxy especially using individual stars. The LMC is a relatively close satellite galaxy of the Milky Way (MW) at 49.9 kpc (van der Marel & Cioni 2001; De Grijs et al. 2014) and so it makes sense to analyze it as it does not pose as many challenges compared to galaxies which are farther away that may or may not be resolved. The second reason is that accurate ages are needed on a star-to-star basis to study the chemical evolution of the LMC at very high resolution.

Galaxies are the sum of their parts and stars make up a large portion of them. With a large enough sample of stars with good spatial coverage, it becomes possible to study the chemical evolution of a galaxy. When a star “dies”, material is ejected into the interstellar medium (ISM) making it available to form newer stars. Thus enriching the reservoir of gas in the ISM to higher metallicities through the yields of the now deceased star. This leads to new stars having elevated chemical abundances and hence higher metallicities. It is also well known that metallicity is a proxy for age. While the particular age-metallicity (AMR) for galaxies will differ, they are an extremely useful tool to study galaxy evolution. The AMR reveals how a galaxy evolved over time. Generally the AMR is measured using clusters or field stars.

Studies of the star formation history (SFH) of a galaxy have the potential to yield AMRs. Usually, observations of resolved stellar population observations are fit with stellar evolutionary models using a combination of distance, age and metallicity parameters. This means that as a result one ends up having a relation between the age and metallicity of stars in the galaxy. Normally though, this method gives very approximate results. For the LMC, there are very few examples where these results are used to draw conclusions about the galaxy’s evolution. Harris & Zaritsky (2009) used the MCPS survey (Zaritsky et al. 1997) to derive SFH across the main-body of the LMC. Because of the shallow nature of the photometric survey, the study was limited to younger ages and only four metallicity bins per single age stellar population. The general conclusions were that the LMC seemed to remain at a constant metallicity in the old ages until around ≈ 4 Gyr ago, when it started to increase to the present day value. A more recent approach with larger photometric depths was used by Meschin et al. (2014), covering three small fields in the LMC. The AMR derived from the SFH results had a good fit with spectroscopic results from field stars by Carrera et al. (2008), but the spatial scope of the study was still relatively small. Furthermore, Weisz et al. (2013) used deep *HST* imaging to derive the SFH in eight fields in the LMC (as well as seven more in the SMC), but released no metallicity information due to the focus being on the comparison of star formation between the two galaxies. In Monteagudo et al. (2018), SFHs for several small fields in the central parts of the LMC were released, but again contained no metallicity information. Ruiz-Lara et al. (2020) used the deep, multi-band, contiguous SMASH data (Nidever et al. 2017) in the LMC to derive spatially-resolved SFHs. The paper was focused on the formation of the LMC’s spiral arm and also did not include any metallicity information. Finally, Mazzi et al. (2021) used infrared VMC data Cioni et al. (2011) covering the entire main body of the LMC. Unfortunately, infrared photometry is even less well suited than optical photometry for metallicity determination because it is less sensitive to metallicity, and the study does not include any AMR results. But they state that populations of stars made up of younger ages should have a lower metallicity than what is predicted from Carrera et al. (2008). This is not to say

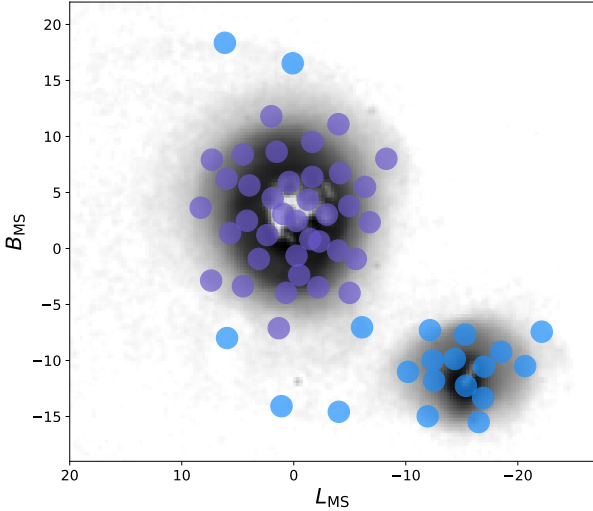


Figure 1. Map of the APOGEE-2 Magellanic Cloud fields (filled circles) and the background showing the density of MC RGB stars selected with Gaia. The LMC fields analyzed here are shown as purple filled circles. For some basic statistics on the LMC fields see Table 2.1.

that infrared photometry should not be used in studies of metallicity. In Choudhury et al. (2021) it was shown that metallicities derived from NIR photometry can be useful in exploring variations across the LMC. Therefore, establishing a precise and reliable source for an LMC AMR will benefit the current literature. Our goal is to take advantage of the precision in our metallicities and the extent of our data to generate an AMR that will cover more areas of the LMC to an unprecedented precision.

Alternatively, there have been many different studies of the LMC that specifically target the calculation of the AMR in the past. For example Olszewski et al. (1991); Dirsch et al. (2000); Grocholski et al. (2006) derive the AMR using clusters, while some papers such as Carrera et al. (2008) derive the AMR using spectroscopy of field stars. Most previous studies have a preference for clusters instead of individual stars and so with the derived individual ages and the known metallicities, we also explore the AMR of the LMC.

One drawback with using clusters for AMR and other age studies is that an age gap exists creating a bimodal cluster age distribution (Da Costa 1991; Geisler et al. 1997). Only two clusters in the LMC have been confirmed having ages between ~ 3 –12 Gyr old. These being ESO 121-SC 03 (Mateo et al. 1986; Olszewski et al. 1991) and KMHK 1592 (Piatti 2022) respectively. Having only two clusters for such a wide range of ages leads to large uncertainties in the behavior of the LMC for intermediate ages. However, Gatto et al. (2020) make the claim using YMCA (Gatto et al. in prep) and STEP Ripepi et al. (2014) data that the gap is observational bias. That work finds 16 candidate intermediate age clusters, which if confirmed will change our understanding of how star clusters formed in the LMC. Currently the only way to get data for intermediate ages is to use field stars to fill in the age gap where clusters are not present or to confirm the existence of more so called age gap clusters.

This paper starts in Section 2 by presenting the four datasets used. Sections 3, 4, and 5 introduce how distances to the individual LMC stars are calculated, the extinction laws used, and the Salaris correction to the metallicity, respectively. Next, Section 7 outlines how the extinctions, ages, and masses are calculated for each star with the validation explained in Section 8. In Section 9, the bias correction

applied to the LMC stars is discussed. Finally, the LMC results are presented in section 10 and discussed in section 11.

2 DATA

2.1 APOGEE

The Apache Point Observatory Galactic Evolution Experiment (APOGEE, Majewski et al. 2017) is a valuable tool to study the LMC. APOGEE is part of the broader Sloan Digital Sky Survey (SDSS IV, Blanton et al. 2017). APOGEE’s main goal is to accurately and extensively study the chemistry and kinematics of the Milky Way (MW). It does this with two identical H -band spectrographs (Wilson et al. 2019) in the northern and southern hemispheres. For the northern hemisphere the spectrograph (APOGEE-N) is located at the Apache Point Observatory (APO) and takes data on the Sloan 2.5 m (Gunn et al. 2006) and NMSU 1.0 m (Holtzman et al. 2010) telescopes. As for the southern hemisphere, the spectrograph (APOGEE-S) is located at the Las Campanas Observatory (LCO) and connected to the du Pont 2.5 m telescope (Bowen & Vaughan 1973).

The raw APOGEE are processed with the data processing pipeline (Nidever et al. 2015) producing 1-D extracted and wavelength calibrated spectra with accurate radial velocities (RVs) determined with Doppler (Nidever 2021). Spectral parameters and abundances are then determined with the APOGEE Stellar Parameters and Chemical Abundances Pipeline (ASPCAP, García-Pérez et al. 2016). This compares the normalized observed spectra with a large grid of synthetic spectra using FERRE (Allende Prieto et al. 2006). The most up-to-date version of the data used in this work is part of SDSS-IV Data Release 17 (Abdurro’uf et al. 2022). In particular for DR17, the APOGEE spectral grid was created using synspec (Hubeny et al. 2021). Updates specific to DR17 can be found in Holtzmann et al. (in prep).

The main ASPCAP spectral fitting determines the “spectral parameters” which affect a significant fraction of the spectrum: T_{eff} , $\log g$, v_{micro} , $[M/H]$, $[C/M]$, $[N/M]$, $[\alpha/M]$, and v_{macro} for giant stars. Individual elemental abundances are then determined from the same spectral grid by holding the spectral parameters constant but varying $[M/H]$ (or $[\alpha/M]$, depending on the element) with the use of narrow spectral windows specific to each element. Chemical abundances provided in DR17 from ASPCAP are: C, C1, N, O, Na, Mg, Al, Si, S, K, Ca, Ti, TiII, V, Cr, Mn, Fe, Co, Ni, and Ce. For this work we extensively use T_{eff} , $[\text{Fe}/H]$, and $[\alpha/\text{Fe}]$ ($=[\alpha/M]+[M/H]-[\text{Fe}/H]$) derived by ASPCAP. Uncalibrated T_{eff} , $\log g$, v_{micro} , $[M/H]$, $[C/M]$, $[N/M]$, $[\alpha/M]$, and v_{sini} can be found in each star’s FPARAM array in the data catalog.

There are both systematic and statistical errors present in the APOGEE data. To minimize the effect of systematic errors, stars with known solar-like metallicity in the solar neighborhood were observed. From these stars offsets were derived and corrected for in the APOGEE data. Statistical uncertainties were calculated by performing multiple visits of single stars and fitting function of T_{eff} , $[M/H]$, and SNR to the observed scatter. More information on α -abundance uncertainties can be found in Nidever et al. (2020).

The LMC selection for DR17 is almost identical to that described in Nidever et al. (2020) for DR16. The biggest difference is the coverage that has been extended to roughly twice the previous size (compare Fig. 1 here to Fig. 1 in Nidever et al. 2020). The quality cuts applied to each field star were:

- $T_{\text{eff_BAD}}$, LOGG_BAD , VMICRO_BAD , ALPHAFe_BAD , CFE_BAD , NFE_BAD , NO_ASPCAP_RESULT flags are not set

- $T_{\text{eff}} < 5200 \text{ K}$
- $\log g < 3.4$
- $S/N > 20$.

After the membership selection and applying the above quality cuts, the total number of stars in the LMC sample is 6130. A CMD and HR diagram for the LMC RGB star sample can be seen in Figure 2.

Detailed information on the APOGEE-1/-2 targeting can be found in Zaslowski et al. (2013) and Zaslowski et al. (2017). APOGEE DR17 has excellent spatial coverage of a significant portion of the LMC as seen in Figure 1 out to a radius $\sim 10^\circ$ (or $\sim 8 \text{ kpc}$). More information on the fields can be seen in Table 2.1.

2.2 Gaia EDR3

The Gaia mission (Gaia Collaboration et al. 2016, 2021) is an extensive space-based all-sky survey. We use both photometric and astrometric data from the early data release 3 (Gaia EDR3), which contains over 1.8 billion sources. Gaia obtains photometric data in three optical bands: denoted BP , G , and RP . All of the Gaia EDR3 data are publicly available online from the Gaia Archive¹. The APOGEE DR17 catalog includes the corresponding Gaia photometry and astrometry columns and much of Gaia EDR3 and Gaia DR3 (Gaia Collaboration et al. 2022) are the same for the LMC stars in this work.

Our age calculations in section 7.2 require uncertainties in the photometric magnitudes. We calculate these from the relative flux uncertainties provided in the data release catalog. Flux and magnitude are related by $m_\lambda = -2.5 \log(F_\lambda)$, where m_λ is the magnitude and F_λ is the flux. Using general error propagation methods and taking into account the zero point for each Gaia band, the magnitude error is given by

$$\sigma_{m\lambda} = \sqrt{\left(\frac{1.085}{F_\lambda/\sigma_\lambda}\right)^2 + zp_\lambda^2} \quad (1)$$

where $\sigma_{m\lambda}$ is the magnitude uncertainty for the λ Gaia band, F_λ/σ_λ is the flux over its error provided by Gaia, and zp_λ is the zero point offset for the band. Plotting the calculated error as a function of the magnitude produces the curve in Figure 3. This was created by taking a large selection of stars and interpolating the error as a function of magnitude. Qualitatively this figure closely resembles the analogous figure in Riello et al. (2021).

Gaia EDR3 includes very accurate proper motions (μ) and parallaxes (ϖ). The reciprocal of the Gaia parallax is used to calculate distances of stars in the APOKASC validation set (see section 2.3). While taking the parallax reciprocal is non-optimal for low-S/N values, the large majority of stars in the APOKASC sample have $S/N \gtrsim 70$ where this is less of a problem.

2.3 APOKASC

APOKASC is a joint spectroscopic and asteroseismic dataset created by combining APOGEE and *Kepler* data (Pinsonneault et al. 2014, 2018). The APOKASC stars have well-determined masses, radii and

ages. We use the APOKASC 3 (Pinsonneault et al. in prep) catalog to validate our estimated ages and masses.

The following selection criteria are applied to the APOKASC data to best match the APOGEE data for the LMC sample:

- $\text{APOKASC3_CONS_EVSTATES} = 1$
- $\varpi/\sigma_\varpi > 3.0$

where $\text{APOKASC3_CONS_EVSTATES}$ denotes RGB stars in the 6.7.4 version of the APOKASC dataset (in contrast to red clump stars). The parallax cut is performed to ensure accurate distances can be found by taking the reciprocal. After the selection criteria is applied, there are 4058 RGB stars left in the APOKASC sample that span T_{eff} from 3712 to 5345. A Kiel diagram of the final selection is shown in Figure 4.

2.4 PARSEC Isochrones

In order to derive extinction, age, and mass estimates of stars we rely on the use of PARSEC (Bressan et al. 2012; Marigo et al. 2017) isochrones, which are available online³. These contain T_{eff} , $\log g$, metallicity, initial mass, the photometric absolute magnitudes, as well as a convenient stellar evolutionary phase label (LABEL). We downloaded a finely-spaced grid of isochrones in age and metallicity for the Gaia EDR3 and 2MASS bands. The ages span 25 Myr to 17 Gyr in steps of 50 Myr, and the metallicities span $[M/H] = -2.3$ to $+0.5$ in steps of 0.02 dex.

3 LMC DISTANCES

The geometry of the LMC disk is well-modeled as a thin, inclined plane. Using this simple model and well-constrained observational parameters, the distances for the LMC disk stars can be calculated. The mathematical basis of this model comes from van der Marel & Cioni (2001) and Choi et al. (2018b).

To calculate the distance in the inclined disk model, the first step is to convert the (α, δ) celestial coordinates to a cylindrical coordinate system (ρ, ϕ) . These coordinates are defined such that ρ is the angular distance from the LMC center (radius) and ϕ is the position angle (east of north). This is analogous to polar coordinates in 2D, but on the celestial sphere. The coordinate conversion to the cylindrical coordinates is:

$$\begin{aligned} \cos \rho &= \cos \delta_0 \cos \delta \cos(\alpha - \alpha_0) + \sin \delta_0 \sin \delta, \\ \sin \rho \cos \phi &= -\cos \delta \sin(\alpha - \alpha_0), \\ \sin \rho \sin \phi &= \cos \delta_0 \sin \delta - \sin \delta_0 \cos \delta \cos(\alpha - \alpha_0), \end{aligned} \quad (2)$$

where $(\alpha_0, \delta_0) = (82.25^\circ, -69.50^\circ)$ is from van der Marel & Cioni (2001).

The distance can be calculated by projecting the angular coordinates onto a plane which means the distance is the given by

$$D = \frac{D_0 \cos i}{\cos i \cos \rho - \sin i \sin \rho \sin(\phi - \theta)}, \quad (3)$$

where $D_0 = 49.9 \text{ kpc}$ (van der Marel & Cioni 2001; De Grijs et al. 2014) is the distance from the Sun to the center of the LMC, $i = 25.87^\circ$ is the inclination of the LMC disk, and $\theta = 149.23^\circ$ is the position angle of the line of nodes. Both the inclination and position angle of the line of nodes comes from the Choi et al. (2018b) analysis of the SMASH (Nidever et al. 2021) red clump stars. When using

¹ <https://gea.esac.esa.int/archive/>

² See <https://www.cosmos.esa.int/web/gaia/dr3-passbands> for these values

³ <http://stev.oapd.inaf.it/cgi-bin/cmd>

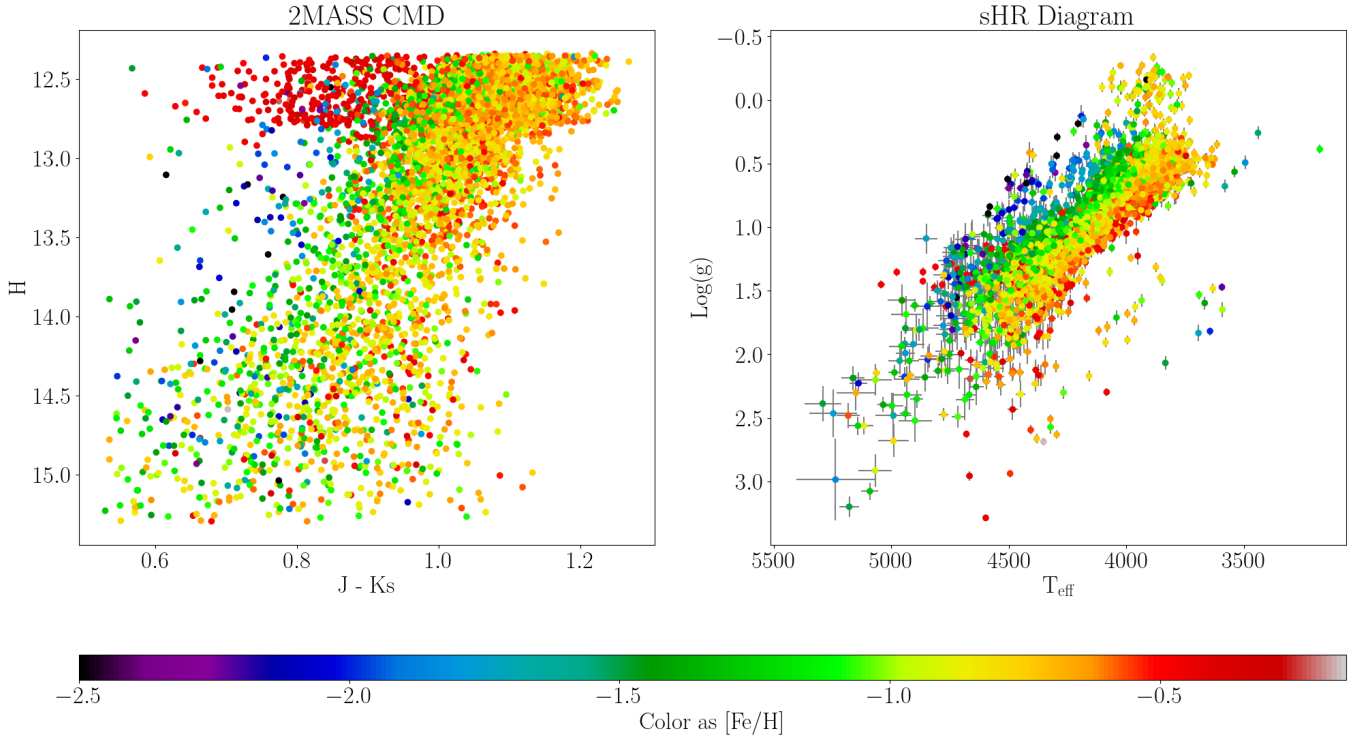


Figure 2. (Left) A 2MASS color magnitude diagram of the selected APOGEE LMC RGB stars colored by [Fe/H]. The tip of the RGB is assumed to be at $H \sim 12.35$ for the LMC (Nidever et al. 2020). (Right) A Kiel diagram for the APOGEE LMC RGB stars colored by [Fe/H].

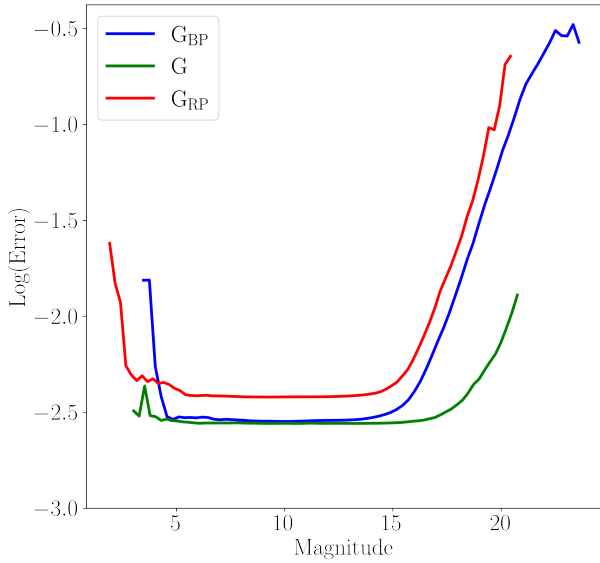


Figure 3. A reproduction of the magnitude error curve for Gaia EDR3 calculated using the Gaia photometry and equation 1. The blue, green, and red curves represent the BP, G, and RP bands respectively. The curves here match qualitatively to the curves in Riello et al. (2021).

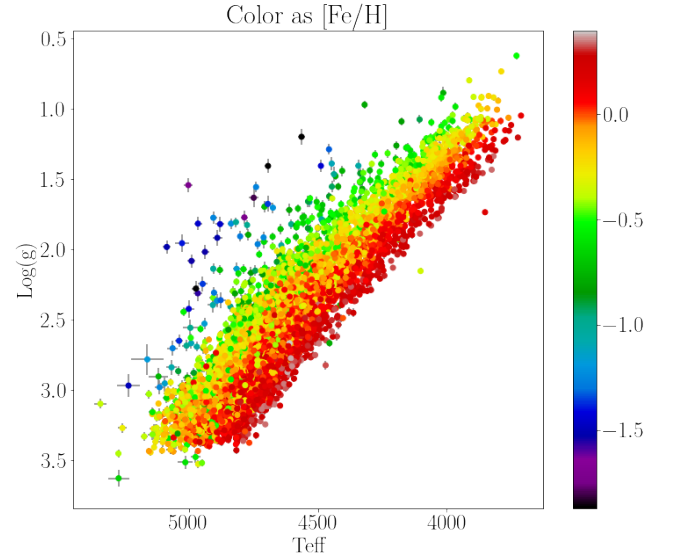


Figure 4. An HR diagram for the selected APOKASC RGB stars colored by [Fe/H].

equation 3, it is important to note that many angle are measured from North and not East, so 90° is added to θ in practice.

We take the equation for finding the radius directly from Choi et al. (2018b), which is

$$r(x, y)^2 = (x \cos \psi - y \sin \psi)^2 + \left(\frac{x \sin \psi + y \cos \psi}{b/a} \right)^2, \quad (4)$$

where ψ ($= 227.24^\circ$) is the position angle of the semi-major axis, and b/a ($= 0.836$) is ratio of the semi-minor axis to the semi-major axis. For angles measured from the north, 90° must be added to ψ just like with θ above. A distance map of the LMC with the added elliptical radius contours (annuli) can be seen in Figure 5.

Table 1. A table of positional data for each of the APOGEE LMC fields including the number of RGB stars observed. R and PA are the projected radius and position angle respectively. N_{Br} is the number of identified bright RGB stars while N_{Fnt} is the number of faint sources (see Section 9).

Name	R.A. (J2000.0)	Decl. (J2000.0)	R (deg)	PA (deg)	N_{RGB}	N_{Br}	N_{Fnt}
30Dor	05:34:3.30	-69:21:6.40	0.8	52.0	41	41	0
LMC1	04:14:32.0	-71:59:22.2	6.3	242.0	169	10	159
LMC2	04:13:14.9	-68:28:21.6	6.7	272.0	148	9	139
LMC3	04:49:10.2	-75:11:48.9	6.1	204.0	188	26	162
LMC4	04:54:54.6	-68:48:6.80	3.1	287.0	254	254	0
LMC5	04:57:10.3	-71:08:54.2	2.9	240.0	236	236	0
LMC6	05:10:55.5	-65:46:21.7	4.4	337.0	200	200	0
LMC7	05:14:46.4	-62:43:22.3	7.3	349.0	171	62	109
LMC8	05:20:48.5	-72:32:48.2	2.8	191.0	220	220	0
LMC9	05:22:15.7	-69:48:1.30	0.7	260.0	143	143	0
LMC10	05:30:28.3	-75:53:11.2	6.1	178.0	171	35	136
LMC11	05:41:49.0	-63:37:17.1	6.4	14.0	195	128	67
LMC12	05:44:9.90	-60:38:40.1	9.4	13.0	138	17	121
LMC13	05:44:24.1	-67:41:59.7	2.7	38.0	173	173	0
LMC14	05:50:34.4	-70:58:29.1	2.2	122.0	152	152	0
LMC15	06:08:2.80	-63:47:24.5	7.3	38.0	175	47	128
LMC16	06:29:7.50	-75:04:58.8	6.9	145.0	131	13	118
LMC17	06:29:59.5	-70:17:23.1	5.3	102.0	176	44	132
LMC18	06:06:28.4	-66:26:29.5	5.0	51.0	192	192	0
LMC19	06:12:35.8	-69:27:47.4	4.0	90.0	182	182	0
LMC20	05:14:31.3	-74:25:36.5	4.7	191.0	208	208	0
LMC21	04:35:3.80	-67:39:8.40	5.3	289.0	205	118	87
LMC22	04:35:47.4	-71:37:2.20	4.7	242.0	205	167	38
LMC23	07:07:56.0	-73:45:55.5	8.6	128.0	86	4	82
LMC24	05:44:24.8	-79:06:12.0	9.3	175.0	70	4	66
LMC25	06:33:14.1	-63:39:58.6	8.9	54.0	170	15	155
LMC26	04:15:7.10	-62:35:31.7	10.1	307.0	65	4	61
LMC27	05:12:55.0	-67:59:33.1	2.3	321.0	152	152	0
LMC28	04:56:36.5	-60:48:53.1	9.6	337.0	185	11	174
LMC29	06:23:21.8	-65:40:18.9	6.7	58.0	210	79	131
LMC30	04:50:5.40	-65:11:22.6	5.9	318.0	205	125	80
LMC31	05:31:58.7	-66:27:10.7	3.5	13.0	152	152	0
LMC32	04:27:18.9	-65:41:49.5	7.1	299.0	221	24	197
LMC33	06:51:56.5	-67:24:9.50	8.1	83.0	180	12	168
LMC34	06:05:43.3	-72:55:21.2	4.4	140.0	201	201	0
LMC35	04:06:26.5	-74:54:2.80	7.9	221.0	160	7	153

4 EXTINCTION LAWS

4.1 Cardelli Extinction Law

In order to calculate and constrain the extinction across multiple bands, we adopt the extinction law directly from [Cardelli et al. \(1989\)](#), hereafter CCM89) for calculating the extinction coefficients.

The extinction relative to the V band can be found with

$$A_{\lambda}/A_V = a_{\text{CCM}}(x) + b_{\text{CCM}}(x)/R_V, \quad (5)$$

where $a_{\text{CCM}}(x)$ and $b_{\text{CCM}}(x)$ are functions of wavelength ($x = 1/\lambda$) with functional forms that vary with the particular wavelength regime (i.e. IR, Optical) and $R_V \equiv A_V/E(B - V)$.

For the IR regime ($0.3 \leq x \leq 1.1 \mu\text{m}^{-1}$), $a_{\text{CCM}}(x)$ and $b_{\text{CCM}}(x)$ are simply

$$a_{\text{CCM}}(x) = 0.574x^{1.61} \quad (6a)$$

$$b_{\text{CCM}}(x) = -0.527x^{1.61}. \quad (6b)$$

For the NIR and Optical regime ($1.1 \leq x \leq 3.3 \mu\text{m}^{-1}$), $a_{\text{CCM}}(x)$

and $b_{\text{CCM}}(x)$ are

$$y(x) = x - 1.82 \quad (7a)$$

$$a_{\text{CCM}}(y) = 1 + 0.17699y - 0.50477y^2 - 0.02427y^3 + 0.72085y^4 + 0.01979y^5 - 0.77530y^6 + 0.32999y^7 \quad (7b)$$

$$b_{\text{CCM}}(y) = 1.41338y + 2.228305y^2 + 1.07233y^3 - 5.38434y^4 - 0.62251y^5 + 5.30280y^6 - 2.09002y^7 \quad (7c)$$

As noted in CCM89, a value of 3.1 for R_V reproduces what would be expected for the diffuse interstellar medium and only starts to substantially deviate from this value in the UV regime ($\lambda < 0.303 \mu\text{m}$). Since we are only considering the optical and IR regimes, $R_V = 3.1$ is used throughout this work unless, otherwise specified.

In this work, the G band extinction (A_G) is taken as the fiducial instead of A_V and this is accomplished by simply dividing Equation 5 by A_G/A_V . A figure of extinctions of all six photometric bands relative to A_G can be seen in Figure 6. The CCM89 extinction law

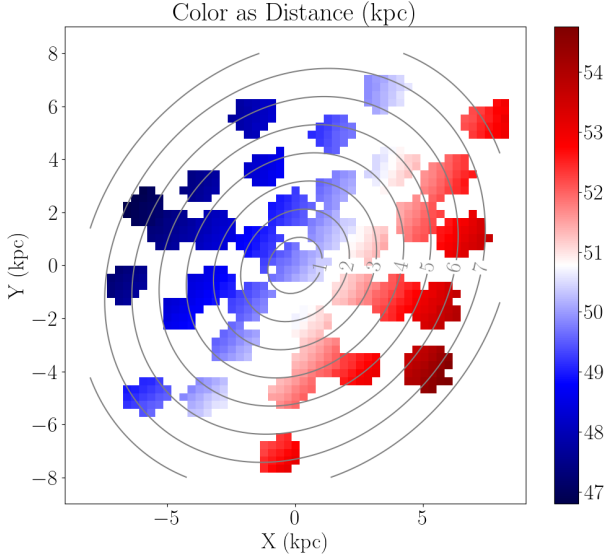


Figure 5. The resulting distance map for the LMC using Equation 3. The contours show lines of constant “elliptical” radius starting at 1 kpc for the center contour out to 8 kpc calculated using equation 6 from Choi et al. (2018b)

is included in the `dust_extinction`⁴ Python package, which is used throughout this work for the actual calculation of the extinction coefficients.

4.2 Fitzpatrick Extinction Law

We make use of a second extinction law to validate the extinctions from Fitzpatrick (1999, hereafter F99). For a more detailed discussion on why F99 is used see Section 8.1. Also, as with CCM89, we make use of `dust_extinction` to calculate the extinction coefficients. While similar to CCM89, F99 gives slightly different results (see Figure 6).

5 SALARIS CORRECTION

Most stellar isochrone models are based on a scaled solar composition, but in actuality stars have a variety of chemical compositions. One solution that allows the use of the solar scaled isochrones for stars with a more complex composition is to shift the $[\text{Fe}/\text{H}]$ of the isochrone based on the star’s $[\alpha/\text{Fe}]$ abundance. Stars that are enhanced in α -elements will appear to have a cooler T_{eff} than expected. This can result in an older age being assigned to the star. Salaris et al. (1993) determined that an α -abundance correction of the following form would fix this:

$$[\text{Fe}/\text{H}]_{\text{sal}} = [\text{Fe}/\text{H}] + \log(a_{\text{sal}}f_{\alpha} + b_{\text{sal}}), \quad (8)$$

where $[\text{Fe}/\text{H}]$ is the uncorrected metallicity, a_{sal} and b_{sal} are coefficients and $f_{\alpha} = 10^{[\alpha/\text{Fe}]}$. The original values for a_{sal} and b_{sal} are 0.638 and 0.362, respectively (Salaris et al. 1993).

For this work we recalculate the a_{sal} and b_{sal} using the solar

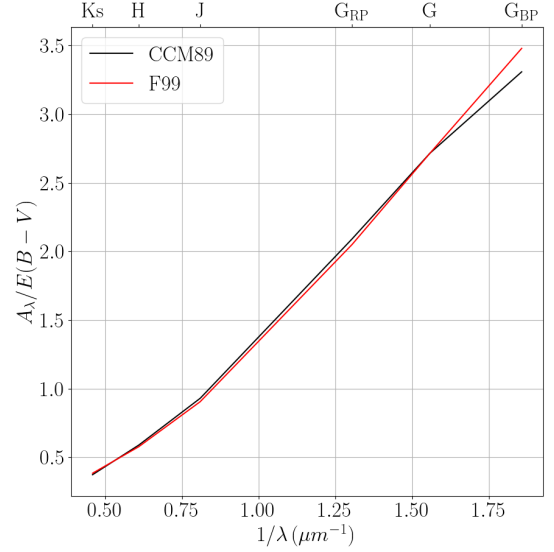


Figure 6. The relative extinction curve of $A_{\lambda}/E(B - V)$ from both CCM89 and F99. The top axis shows the different photometric filters used in this work.

composition from Asplund et al. (2021). Calculating the coefficients is done using

$$a_{\text{sal}} \equiv \sum_X \left(\frac{X}{Z} \right) = \sum_X 10^{\log \epsilon_X - 12.0} \frac{A_X}{A_H} \left(\frac{Z}{X} \right)_{\odot}^{-1} \quad (9a)$$

$$b_{\text{sal}} = 1 - a_{\text{sal}} \quad (9b)$$

where $\log \epsilon_X$ is the value reported in Asplund et al. (2021), A_X/A_H is the atomic mass ratio of element X to hydrogen from IUPAC⁵ (not to be confused with the relative extinction coefficients used elsewhere in this work), and $(Z/X)_{\odot}$ is the Asplund et al. (2021) value of 0.0187 ± 0.0009 . The sum is over the exact same elements used in Salaris et al. (1993) (i.e. O, Ne, Mg, Si, S, Ca). The new updated values for the correction are $a_{\text{sal}} = 0.659$ and $b_{\text{sal}} = 0.341$.

6 CALIBRATIONS

6.1 Effective Temperature

Having an accurate temperature for a star is critical as the calculation of ages and extinctions in Section 7 relies heavily on this value. It is also important that the observed T_{eff} and isochrone T_{eff} values agree with each other. We find that the results from our age validation sample is greatly improved when the temperatures provided by APOGEE are recalibrated and the “named” TEFF values are not used directly.

Here we outline how the recalibration was performed with the stars in a two step process by using PARSEC isochrones and low extinction RGB stars in the full APOGEE allStar summary file⁶. RGB stars were used for the calibration as the LMC stars should be RGB. First, the RGB stars were selected using the criteria

- uncalibrated $\log(g) < 3.5$

⁵ <https://iupac.qmul.ac.uk/AtWt/>

⁶ https://www.sdss.org/dr17/irspec/spectro_data/

⁴ <https://dust-extinction.readthedocs.io/en/stable/#>

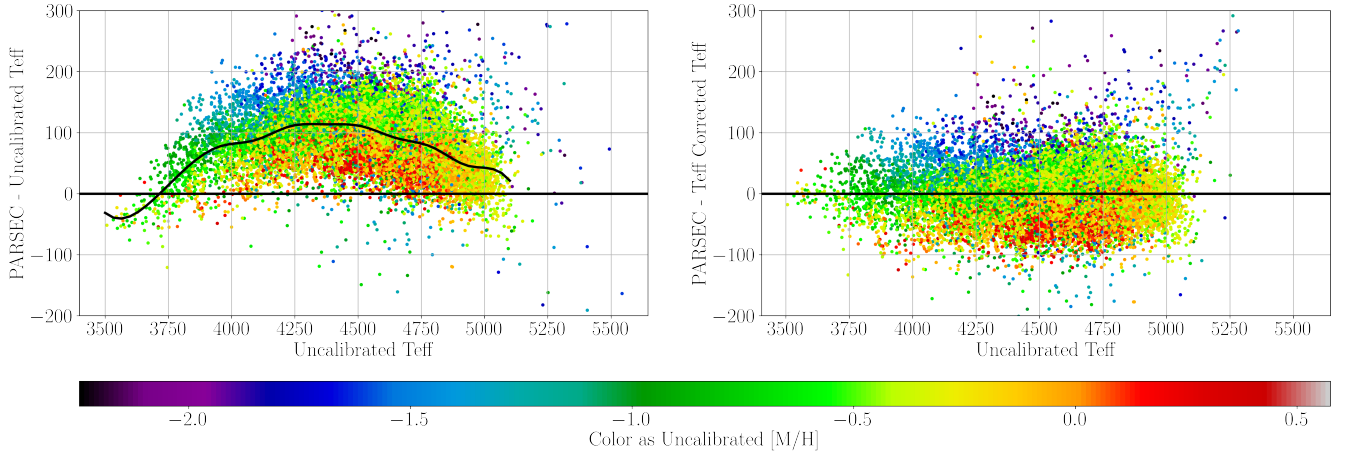


Figure 7. (Left) The residuals of the photometric and uncalibrated ASPCAP T_{eff} values with the spline used to temperature correct the uncalibrated T_{eff} . (Right) The residuals after the T_{eff} correction has been applied. There is a clear trend in $[M/H]$ and so a second spline as a function of $[M/H]$ has been applied (see the text and Figure 8).

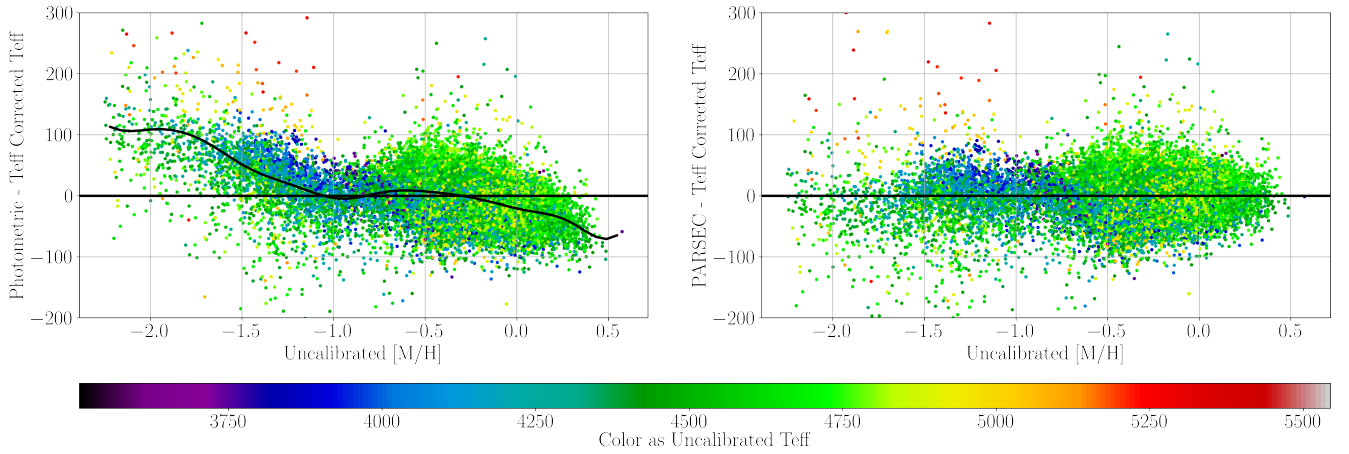


Figure 8. (Left) A plot of the residuals between the photometric and T_{eff} -corrected spectroscopic T_{eff} values (T_{eff} spline applied) with the spline used to $[M/H]$ correct the T_{eff} values. (Right) The residuals after the $[M/H]$ correction has been applied. The median residual after the $[M/H]$ has been applied is -1.72 K with a scatter of 23.75 K.

- uncalibrated $T_{\text{eff}} < 6000$ K

where the uncalibrated $\log(g)$ and T_{eff} values can be found in the `FPARAM` column in the `allStar` file. This selection does not remove red clump (RC) stars, which were identified and removed using

- $2.38 < \text{uncalibrated } \log(g) < 3.5$
- $[C/N] > 0.04 - 0.46[M/H] - 0.0028 \cdot dT$

where

$$dT = T_{\text{eff,spec}} - (4400 - 552.6 \cdot (\log g_{\text{spec}} - 2.5) - 324.6 \cdot [M/H]) \quad (10)$$

where $T_{\text{eff,spec}}$, and $\log g_{\text{spec}}$ are `Teff_SPEC` and `LOGG_SPEC` in the `allStar` file, respectively. These are the same RGB selection criteria from DR16 used for the T_{eff} calibration (Jönsson et al. 2020). Any star with a non-zero `ASPCAPFLAG` value was removed to create a “pristine” sample of RGB stars. The pristine sample overlaps the RGB stars in both the `APOKASC` and the selected LMC RGB datasets in $T_{\text{eff}} - \log g - [Fe/H]$.

Once the RGB stars were selected, low extinction stars were picked

out such that $\text{SFD_EBV} \leq 0.03$, where SFD_EBV is the $E(B - V)$ value from Schlegel et al. (1998). In actuality, the value of the cutoff is unimportant so long as it is small so that the attenuation due to the reddening is negligible when calculating the intrinsic color for calibration. There are some regions where the Schlegel map does not give accurate values for reddening, such as the center of the LMC. It is assumed that the calibration RGB stars cover enough of the sky where the Schlegel map is accurate that stars in places where this is not true can still be calibrated with the method in this section.

Even after making the necessary cuts to create a sample of RGB stars, there are still some RC stars remaining. These stars are easily removed because they do not follow the expected RGB trend in $\log g - T_{\text{eff}} - [Fe/H]$ space.

Next, the photometric temperatures were calculated for the sample of low extinction RGB stars using the PARSEC isochrones through the following process:

- Pick all isochrones with the Salaris corrected metallicity of the star.
- Remove extremely old ($10 \text{ Gyr} < \text{age}$) or young ages ($\text{age} >$

0.5 Gyr). Age in itself does not greatly impact the color- T_{eff} relation for the isochrones.

(iii) The isochrone color- T_{eff} relation is interpolated using a B-spline for each of the colors (i.e., $BP - G$, $G - RP$, $G - J$, $G - H$, and $G - K_s$).

(iv) The “photometric T_{eff} ” for each star is then calculated using the weighted mean of the T_{eff} values from the individual colors.

Calibrating the T_{eff} values involves fitting residuals between the photometric and spectroscopic temperatures. We find the best way to calibrate the T_{eff} values is a two-step process. The first step is fitting a spline as a function of the uncalibrated spectroscopic T_{eff} values to the median residuals (photometric T_{eff} – uncalibrated spectroscopic T_{eff}). In this case, the spline is fit to the binned median values. Figure 7 shows the T_{eff} residuals before and after of this first step. After this initial correction there is a trend in $[M/H]$ that is still present and, therefore, the second step is to fit a second spline as a function of uncalibrated $[M/H]$ to the median residuals of the photometric T_{eff} and the T_{eff} -corrected spectroscopic T_{eff} . Figure 8 illustrates this second step. In the end, the final photometric and calibrated spectroscopic T_{eff} residuals have a median of -1.72 K and scatter of 23.75 K. The splines derived from fitting the residuals were then used to calculate the T_{eff} values for the datasets on this work.

6.2 APOKASC Ages

The ages presented in the APOKASC catalog were derived using isochrones from the Yale Rotating Evolution Code (YREC, Pinsonneault et al. 1989; Van Saders & Pinsonneault 2012) or the Garching Stellar Evolution Code (GARSTEC, Weiss & Schlattl 2008) not the PARSEC isochrones as we use here. For consistency’s sake, we re-derive ages for the APOKASC stars using their APOKASC-determined mass, the star’s Salaris corrected metallicity, and the PARSEC isochrones using the following procedure:

- (i) All isochrones with the two closest metallicity values to the star’s own Salaris corrected metallicity are selected.
- (ii) For both the lower and higher metallicities, the age is interpolated as function of mass for the APOKASC-mass value of the star.
- (iii) The ages for the lower and higher metallicities are linearly interpolated to the star’s Salaris corrected metallicity giving its final age.

The calculation of the APOKASC ages using the PARSEC models and the APOKASC 3 masses versus the original APOKASC 3 ages do differ slightly. On average the re-derived APOKASC ages tend to be younger. The youngest ages remain relatively unchanged while for the oldest ages the deviation is ~ 1.75 Gyr.

7 EXTINCTION, AGE, & MASS CALCULATION

7.1 Extinction Calculation

Extinction is the attenuation of the flux of a star due to dust and gas between the observer and the star. This needs to be accounted for in order to produce accurate absolute photometry as the age method described in Section 7.2 depends sensitively on the photometry.

An important quantity directly related to the extinction is the reddening. The reddening of a stars is the color excess due to different amounts of extinction in two different bands.

$$E(G - K_s) = (G - K_s)_{\text{obs}} - (G - K_s)_{\text{int}} = A_G - A_{K_s} \quad (11)$$

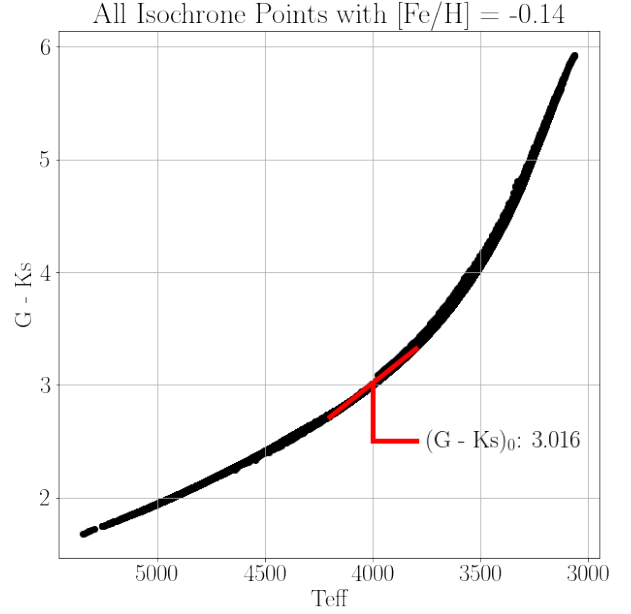


Figure 9. An example of how the intrinsic colors are determined from the isochrone photometry- T_{eff} relations.

Using the G band as the fiducial, all other reddenings for each of the colors are coupled. The reddening equations can be re-framed as a linear algebra problem and solved for A_G :

$$A_G = \frac{\mathbf{A}'(\lambda) \cdot \mathbf{E}(\lambda)}{|\mathbf{A}'(\lambda)|^2} \quad (12a)$$

$$\mathbf{A}'(\lambda) = \begin{cases} \frac{A_{BP}}{A_G} - 1 & \text{if } \lambda = BP \\ 1 - \frac{A_\lambda}{A_G} & \text{if } \lambda \neq BP \end{cases} \quad (12b)$$

$$\mathbf{E}(\lambda) = \begin{cases} E(BP - G) & \text{if } \lambda = BP \\ E(G - \lambda) & \text{if } \lambda \neq BP \end{cases} \quad (12c)$$

where the $\frac{A_\lambda}{A_G}$ can be found using an extinction law such as CCM89, and the components of $\mathbf{E}(\lambda)$ are the reddenings for each color.

The intrinsic color of a star can be found by interpolating isochrones with the following process:

- (i) Pick isochrones with the Salaris corrected $[Fe/H]$ of the star.
- (ii) Select all isochrone points with a temperature within 200 K of the star’s T_{eff} .
- (iii) The isochrone colors for $BP - G$, $G - RP$, $G - J$, $G - H$, and $G - K_s$ are interpolated as functions of temperature using a B-spline.
- (iv) Plugging in the T_{eff} value of the star gives the expected intrinsic value for each of four colors previously mentioned and reddening is found. A pictorial example of calculating the $G - K_s$ intrinsic color can be seen in Figure 9.

Once A_G is calculated for a star, the chosen extinction law is used to calculate the extinction for all the other bands. The age of a star has a negligible effect on the color- T_{eff} relationship, therefore, it is not considered when determining the extinction.

7.2 Age Calculation

The age of a star can be determined by comparing the observed photometric and spectroscopic parameters to stellar isochrones. Specif-

ically, the absolute multiband photometry is the most sensitive parameter to age. Given a star's T_{eff} and Salaris-corrected $[\text{Fe}/\text{H}]$, we compare the observed multiband absolute magnitudes and surface gravity to the isochrones to determine age.

7.2.1 Interpolated Isochrone Parameters

Within our isochrone grid, which is finely-sampled in $[\text{Fe}/\text{H}]$ and age, we must interpolate a number of properties both “along” the isochrone (i.e., in mass) or between the grid points (in $[\text{Fe}/\text{H}]$ and age). The PARSEC isochrones provide an `int_IMF`⁷ column which is the indefinite integral of the IMF (initial mass function) by number from zero to the current mass. The difference in `int_IMF` between two neighboring isochrone points ($\Delta\text{int_IMF}$) provides the number of stars occupying that isochrone segment (or stellar mass) per unit mass of the total initial stellar population. For our purposes, $\Delta\text{int_IMF}$ essentially gives the expected number of RGB versus AGB stars or their relative probability. More information about why $\Delta\text{int_IMF}$ is important see section 7.4 The isochrone absolute magnitudes, $\log g$, and $\Delta\text{int_IMF}$ for a given age are interpolated through the following process:

- (i) Pick all isochrone points with the Salaris-corrected $[\text{Fe}/\text{H}]$ of the star regardless of age.
- (ii) Determine an initial guess for the age by calculating χ^2 using BP , G , RP , J , H , K_s , T_{eff} , and $\log g$ (see Eq. 13) for all selected isochrone points and picking the one with the lowest χ^2 value.
- (iii) Determine the closest two adjacent ages of the initial guess age. If no isochrone points exist for the chosen age and $[\text{Fe}/\text{H}]$, then pick the next closest age.
- (iv) Remove all isochrone points outside a specified T_{eff} range as these points should not affect the interpolations. For most stars this amount to keeping isochrone points within 200 K of the measured T_{eff} of the star.
- (v) For each of the two ages the T_{eff} –magnitude relationship for each band, T_{eff} – $\log g$, and T_{eff} – $\Delta\text{int_IMF}$ relationships are used to interpolate these quantities for the star’s observed T_{eff} .
- (vi) Finally, the two sets of interpolated isochrone quantities are linearly interpolated in age for the desired age.

Normally, the T_{eff} –magnitude relationship for any given $[\text{Fe}/\text{H}]$ exhibits a large degeneracy. However, this degeneracy can be broken with age as seen in Figure 10. This work exploits this to obtain the age of a star because the photometry and T_{eff} are known. Also the boundary between the RGB and AGB phases can be blurred due to uncertainty in the T_{eff} or magnitude values of a star as well as the close proximity of RGB and AGB isochrone points. The overlap is illustrated in Figure 10. This means that it is possible either RGB or AGB isochrones points could potentially describe a star due to overlap and the true evolutionary phase of a star is uncertain (see Figure 10).

If the age is considered a free parameter, then it can be found by fitting the isochrone absolute magnitudes, and $\log g$ and matching to the observed absolute magnitudes and surface gravity. To accomplish this we make use of `scipy.optimize.curve_fit` (hereafter `curve_fit`). We limit the maximum number of iterations in `curve_fit` to 5000.

The best age is determined by looking at the χ^2 value for the final photometry and $\log g$ determined by `curve_fit`. Here the χ^2 value is calculated by

$$\chi^2 = \sum_{\lambda} \left(\frac{m_{\lambda,\text{iso}} - m_{\lambda,\text{obs}}}{\sigma_{\lambda,\text{obs}}} \right)^2 + \left(\frac{\log g_{\text{iso}} - \log g_{\text{obs}}}{\sigma_{\log g,\text{obs}}} \right)^2, \quad (13)$$

where $m_{\lambda,\text{iso}}$ is the isochrone apparent magnitude for the λ band (i.e., BP , G , RP , J , H or K_s), $m_{\lambda,\text{obs}}$ is the observed apparent magnitude, and $\sigma_{\lambda,\text{obs}}$ is the measured uncertainty in the observed λ band magnitude. The second term is the $\log g$ contribution to the χ^2 where $\log g_{\text{iso}}$ is the value predicted from the isochrone interpolation, $\log g_{\text{obs}}$ is the observed surface gravity, and $\sigma_{\log g,\text{obs}}$ is the uncertainty in the observed value of the surface gravity. The additional $\log g$ term in χ^2 produces improved fits and uses all of the observed information.

7.3 Mass Calculation

The mass and age of a star are highly anti-correlated on the RGB, which means it is generally straightforward to calculate the mass of a star if its age is known and vice versa. There is a slight degeneracy in the age-mass relationship that is broken with $[\text{Fe}/\text{H}]$, which is a known quantity for our stars. At an age of 10 Gyr the isochrones mass can vary up to about $\pm 0.28 M_{\odot}$ and at an age of 1 Gyr the isochrones mass can vary up to about $\pm 0.33 M_{\odot}$. To determine the mass for a star, it is interpolated as a function of age for a given Salaris-corrected $[\text{Fe}/\text{H}]$.

7.4 Evolutionary Phase Weighting

While most of the stars in our sample are RGB stars, there should also be a small amount of “contamination” from other phases of evolution such as the AGB. The tip of the APOGEE RGB (TRGB) selection is at a magnitude of $H \sim 12.35$, but there can be overlap between the AGB and RGB regions in color magnitude space close to this magnitude (Nidever et al. 2020). Figure 10 shows $[\text{Fe}/\text{H}] = -0.14$ isochrones in the G – T_{eff} plane for a range of ages. Only the RGB phase is displayed in the left panel which shows a sizeable gap between the older ages (> 1.0 Gyr) and very young ages ($\lesssim 1$ Gyr). There are stars in our APOGEE sample that fall in that gap. As can be seen in the right panel, this gap is “filled” with the AGB phase with some overlap with the RGB. Since there is no easy way to separate the RGB and AGB stars in our sample, we take a weighted sum between the ages calculated for RGB and AGB points.

This phase weighting is done through the following process:

- (i) The age and mass for each star is calculated for each phase (RGB and AGB) separately without allowing for extrapolating outside the specified T_{eff} range as described in Sections 7.2 and 7.3.
- (ii) If a star is covered by only one phase, then that age and mass are used. If a star is covered by both phases, then the mean of the RGB and AGB mass and age values are calculated weighted by each phase’s $\Delta\text{int_IMF}$.
- (iii) If neither phase covers the star within the specified T_{eff} range, then the code is allowed to extrapolate up to a limit of 200 K. A star is assigned a “bad” value if it is beyond this 200 K extrapolation limit.

$\Delta\text{int_IMF}$ represents the number of stars in a 1 solar mass total stellar population between the two points of the integrated IMF (`int_IMF`). This can be thought of as the probability of detecting a star in this phase.

The `int_IMF` is provided as part of the isochrone table from PARSEC and we use the Kroupa IMF (Kroupa 2001; Kroupa 2002). The $\Delta\text{int_IMF}$ is chosen for the weighting factor as it naturally

⁷ Previously called FLUM.

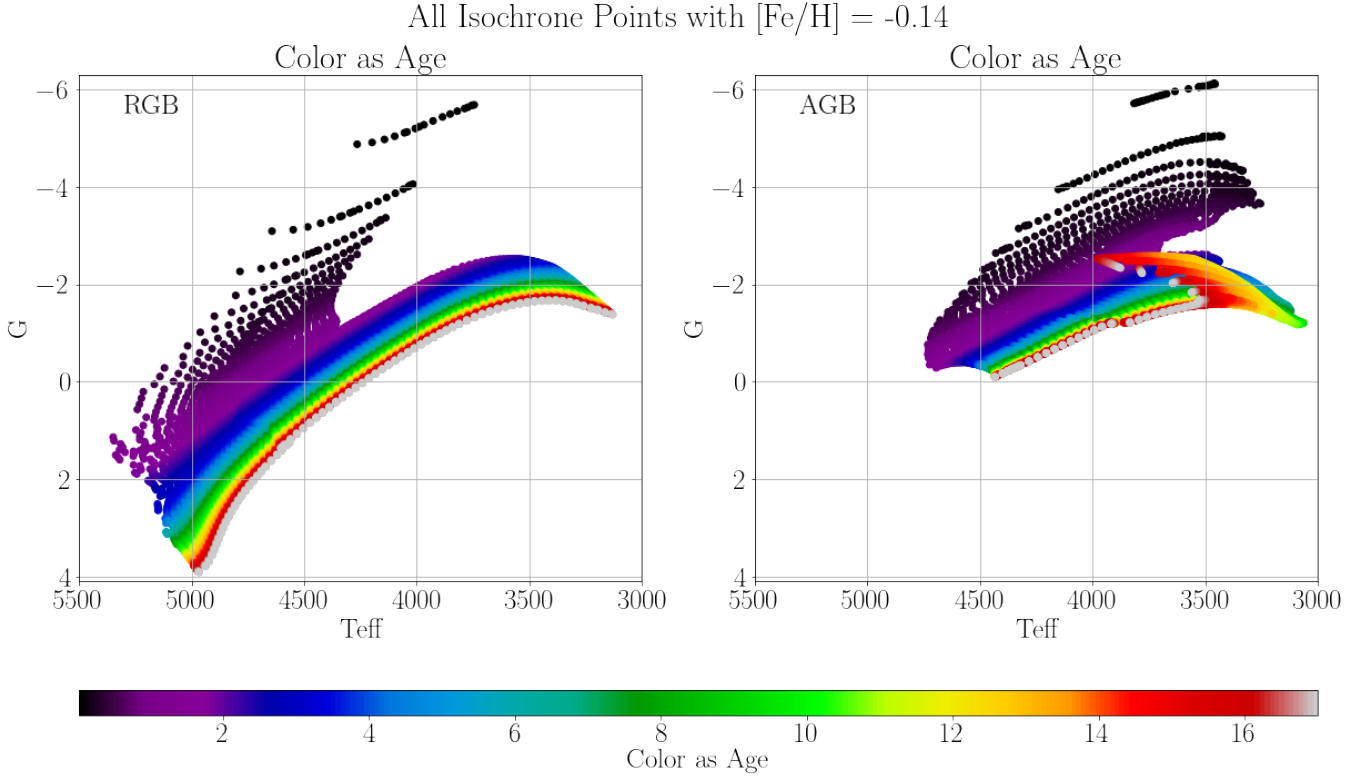


Figure 10. (Left) The G - T_{eff} relationship for $[\text{Fe}/\text{H}] = -0.14$ for the RGB isochrone points. There is a lot of degeneracy in the magnitude- T_{eff} relation, but clearly broken with age. This is the basis for using the interpolations in section 7.2 to get the ages. (Right) The same as the left panel, but for the AGB isochrone points. The AGB points mostly cover the gap in the RGB isochrone points between the young branch the rest of the points.

encodes the fact that there should be more RGB stars compared to AGB stars.

8 APOKASC VALIDATION

We use the APOKASC dataset to validate and calibrate our ages since it has highly accurate asteroseismic ages and uses an independent technique. The method used by APOKASC to derive ages relies on calculating the mass using temperature and asteroseismic scaling relations to obtain a measured surface gravity with APOGEE $[\text{M}/\text{H}]$ and $[\alpha/\text{M}]$. An evolutionary track is then used for the corresponding mass, $[\text{M}/\text{H}]$ and $[\alpha/\text{M}]$. The age of a star is then found by determining the point on the evolutionary track that has a $\log g$ value equal to the asteroseismic $\log g$. While the APOKASC method does rely on measured APOGEE DR16 (Ahumada et al. 2020) values of T_{eff} , $[\text{M}/\text{H}]$, and $[\alpha/\text{M}]$, the rest of the method is completely independent. This method applies to the APOKASC 3 ages in the A3P_AGE MOD_JT column. For more on previously calculated ages included with the APOKASC catalog, which may rely on slightly different methods, please see Serenelli et al. (2017) or Pinsonneault et al. (2018).

8.1 APOKASC Extinctions

Accurate photometry is required to calculate the age of a star and, therefore, is important that the star's extinction is well-determined. The APOGEE catalog includes the Schlegel et al. (1998) $E(B - V)$ value for every star. We follow Schlafly et al. (2010) in converting

the Schlegel reddening values to extinctions for any band with a correction factor:

$$A_{\lambda} = \begin{cases} 0.78/1.32 \times E(B - V)_{\text{SFD}} \times \frac{F_{99}(\lambda)}{F_{99}(1\mu\text{m})} & \text{if } E(B - V) > 1 \\ 0.78 \times E(B - V)_{\text{SFD}} & \text{if } E(B - V) < 1 \end{cases} \quad (14)$$

where $E(B - V)_{\text{SFD}}$ is the Schlegel reddening value, $F_{99}(\lambda)$ is the value of the Fitzpatrick (1999) extinction law for the λ band and $F_{99}(1\mu\text{m})$ is the Fitzpatrick (1999) extinction law value for a wavelength of $1\mu\text{m}$.

Comparing the A_G expected from Schlegel et al. (1998) to the calculate A_G in Figure 11 shows good agreement with a slight offset of about 0.043 mag. The part of the Kepler field nearest the MW plane tends to agree less well than the rest of the field. However, this is a good validation of the extinction values derived from our method.

8.2 APOKASC Ages

While our derived ages rely on using the PARSEC isochrones, the APOKASC method did not use PARSEC models in their calculations to convert mass to age. This means that a direct comparison of our ages to the APOKASC catalog ages might have discrepancies because of the use of different models. Instead, we use the Salaris-corrected $[\text{Fe}/\text{H}]$ and the APOKASC mass to determine the ages by interpolating the PARSEC isochrones. This is very similar to the mass calculation described in Section 7.3, but essentially in reverse.

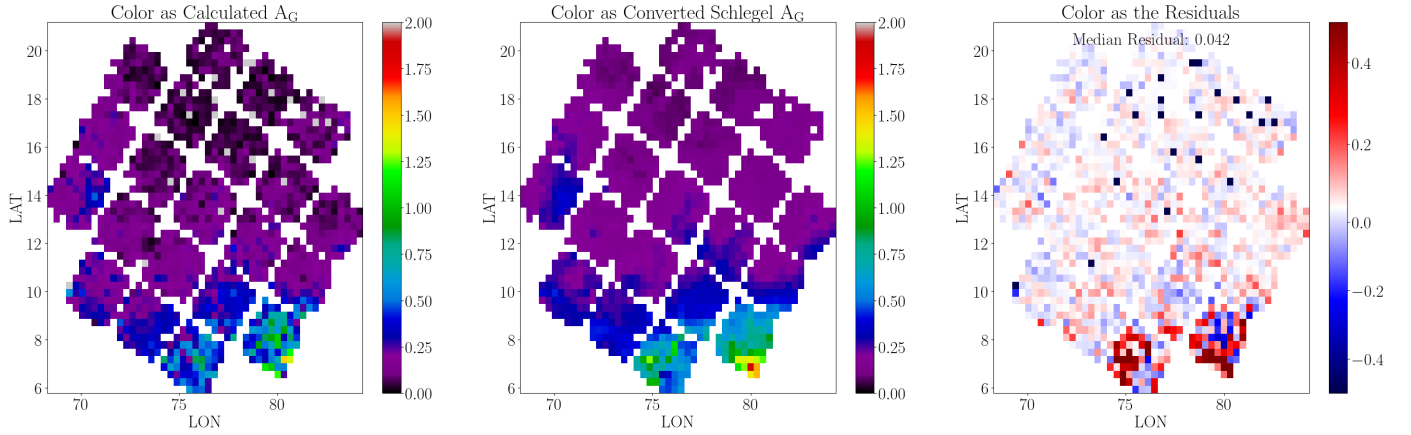


Figure 11. (Left) A_G extinction map converting the Schlegel et al. (1998) reddening values using Schlafly et al. (2010) and Fitzpatrick (1999). (Center) A_G map using the values calculating using the method in this work. (Right) The residuals between the Schlegel and calculated A_G values with a median residual of 0.043 mag.

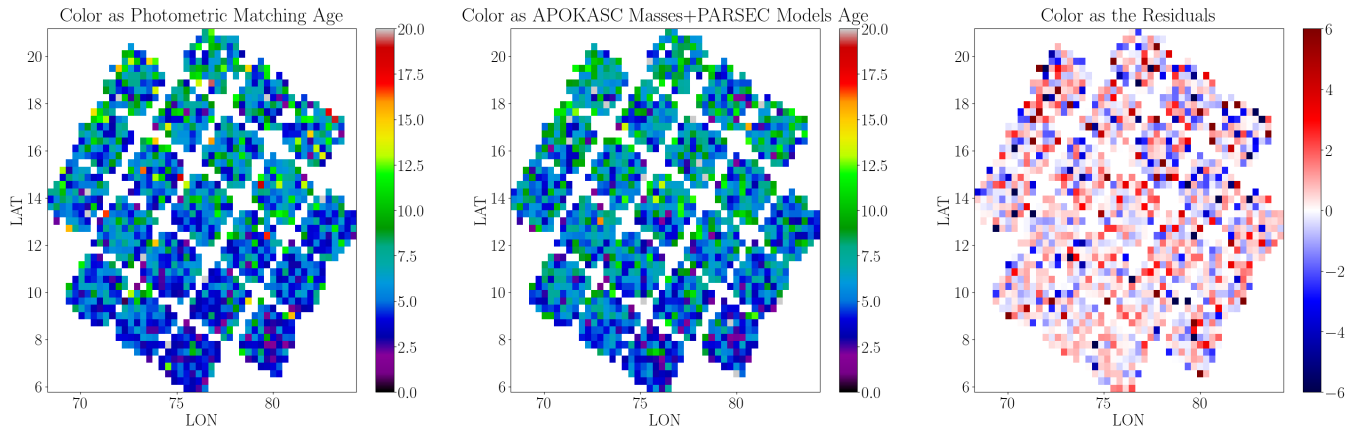


Figure 12. (Left) Age map of the Kepler field using APOKASC 3 masses and PARSEC isochrones. (Center) Age map of the Kepler field calculated using our method described in Section 7.2. (Right) The residuals between the methods with a median residual of 0.2 Gyr.

From now on, we shall call these ages derived from the APOKASC mass and PARSEC isochrone the “APOKASC ages”.

Comparing the APOKASC ages and our ages calculated through the photometric matching process described in Section 7.2 shows quite good agreement. Figure 12 shows the spatial map of the Kepler field ages from the two methods as well as the difference. Visually, the maps look very similar and the right panel showing that the residuals have an average close to zero, as desired.

A direct one-to-one comparison of the APOKASC ages against our ages shows more clearly how well the two methods agree (see Figure 13). Overall, the locus of the stars in the 2D histogram is very close to the one-to-one line. Ages under 10 Gyr typically agree better and especially under ~ 8 Gyr. This is not unexpected as older ages have larger uncertainties because the isochrones tend to stack up on each other in color–magnitude space. A curious feature is the upturn that happens for APOKASC ages older than about 10 Gyr. While we have investigated various causes for this systematic behavior, its origin remains unclear. This is not as bad as it seems, because there are few stars older than 10 Gyr. However, it does cause a larger spread of our oldest ages.

As for systematic uncertainties, we find that the dispersion in the residuals is ~ 1 Gyr for younger stars and then increase linearly up to

about 3 Gyr for older stars close to the age of the universe. This is a roughly $\sim 20\%$ age uncertainty.

8.3 APOKASC Masses

The mass and age of a star can be related through the mass–age relation. As another check this relation can be used to validate the ages. If the ages are correct then the masses calculated should match closely to the APOKASC catalog mass. After calculating the masses using section 7.3, the mass-to-mass plot in Figure 14 shows good agreement. The locus of the stars in that plot match very well with the 1-to-1 black line. The number of stars in each bin quickly fall off moving from the line. The derived mass calculated from the photometric matching method appear to be slightly higher than APOKASC 3 values. Nonetheless, this is a reassuring result and suggests that the age calculation method in section 7 works well.

9 BIAS CORRECTION

There are a number of biases in our dataset that need to be corrected for to obtain reliable age-related measurements. There are two main

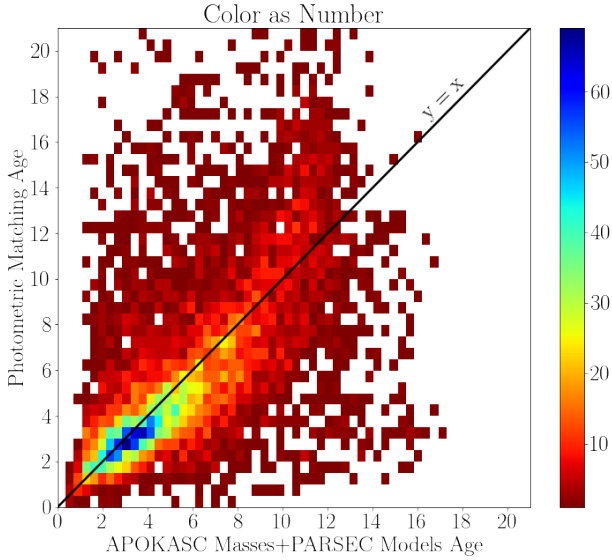


Figure 13. An age-to-age plot comparing the ages derived using the APOKASC masses and PARSEC models and ages derived using the photometric matching described in section 7.2 for the APOKASC validation set colored by the number of stars in each bin. To help guide the eye the 1-to-1 line has been overplotted in black. It is clear especially for younger stars that the photometric matching ages tend to be slightly younger, though overall there is quite good agreement.

biases that we correct for: (1) the targeting selection function, and (2) the number of expected RGB and AGB stars in our target selection box as a function of age and metallicity.

In general, one is not able to spectroscopically target and observe all of the stars in a given target selection category. This was also the case for the APOGEE-2S Magellanic Cloud fields. Our main goal was to obtain an integrated $S/N=100$ (over all visits) for a given star. The LMC fields were allotted nine \times ~ 1 hour visits which meant that the $S/N=100$ could be achieved for $H \leq 12.8$ stars. Therefore, the main RGB targeting category (BrtrRGB) was from $H=12.0$, the nominal tip of the RGB, to $H=12.8$. In the inner fields, there were many more BrtrRGB targets than could be accommodated by the APOGEE spectrograph (~ 250 science targets per plate). This required us to select a subset of the targets which was accomplished by randomly drawing 260 stars (allowing for a small buffer to account for fiber “collisions”). In the outer fields, with lower stellar density, there were often less than 260 targets in the BrtrRGB box, and, therefore, fainter targets (FntRGB) were included to fill the shortfall. The faint limit was extended only as faint as was needed to fill the 260 number of targets. Therefore, the faint limit in the outer fields varies from field to field and extends in some cases to $H=15.3$. For each field we calculate an average “selection function” which is calculated as

$$\text{Selection Function} = \frac{N_{\text{potential targets}}}{N_{\text{observed targets}}} \quad (15)$$

For consistency and simplicity across all fields, we use $N_{\text{potential targets}}$ for all targets down to $H=15.3$. The outer fields have selection function values near unity, while the inner fields have very large values indicating that only a small fraction of the potential targets were observed.

From stellar evolution models we know that the number of RGB stars in a given magnitude range of a stellar population is not constant but varies systematically with age and metallicity. This adds a separate “astrophysical” bias, which is especially important when

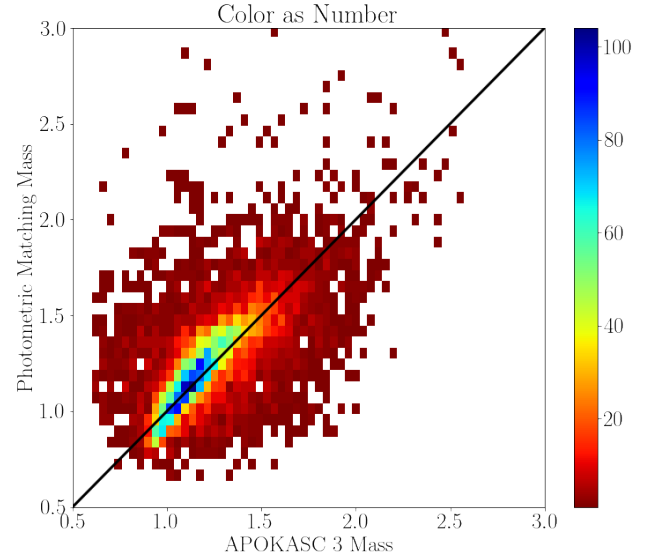


Figure 14. Comparing the APOKASC 3 masses to the masses calculated using Section 7.3.

using age histograms, because variations are expected even if the star formation history is constant. We correct for this bias by calculating the number of stars expected in our target selection boxes for a given age and metallicity, $N_{\text{stars}}([\text{Fe}/\text{H}], \text{Age})$, using synthetic photometry generated from PARSEC isochrones. We use a total stellar population of $10^8 M_{\odot}$ and the RGB, horizontal branch, and AGB evolution stages. As described above, the PARSEC $\Delta \text{INT_IMF}$ value is used to ascertain the number of synthetic stars to produce along the isochrone. The left panel of Figure 15 shows the number of stars falling in the target selection box as a function of metallicity and age while the middle and right panels show average values for age and metallicity, respectively. A substantial amount of structure is seen for younger ages, with a peak at ~ 0.15 Gyr and a “valley” for 0.3–1.5 Gyr. These are significant biases that need to be accounted for.

For a given star, we want to determine the amount of stellar population mass (M_{SP}) that this star “represents”. We convert our number of stars in the target selection box as a function of age and metallicity, $N_{\text{stars}}([\text{Fe}/\text{H}], \text{Age})$, into a stellar population mass by taking the total stellar mass ($10^8 M_{\odot}$) used to generate our synthetic photometry (described in the previous paragraph) and dividing by the expected number of stars in the target selection box:

$$M_{\text{SP}}([\text{Fe}/\text{H}], \text{Age}) = \frac{10^8 M_{\odot}}{N_{\text{stars}}([\text{Fe}/\text{H}], \text{Age})} \quad (16)$$

Note, that our synthetic photometry did not distinguish between RGB or AGB stars but just counted all stars falling into our target selection box. This deals nicely with the evolutionary phase ambiguity mentioned above.

When determining M_{SP} for a given star, we take into account the uncertainty in its age and metallicity by using a “measurement” probability distribution function ($P_{\text{meas}}([\text{Fe}/\text{H}], \text{Age})$) unique for each star and represented as a 2-D Gaussian:

$$P_{\text{meas}}([\text{Fe}/\text{H}], \text{Age}) = \mathcal{N}([\text{Fe}/\text{H}]_0, \sigma_{[\text{Fe}/\text{H}]}) \times \mathcal{N}(\text{Age}_0, \sigma_{\text{Age}}) \quad (17)$$

where $\mathcal{N}()$ is the normalized Gaussian distribution. In addition, we can use $N_{\text{stars}}([\text{Fe}/\text{H}], \text{Age})$ itself as a probability distribution function, i.e. a prior. Regions of higher values indicate that we are more likely to detect stars there than regions where the values are low or

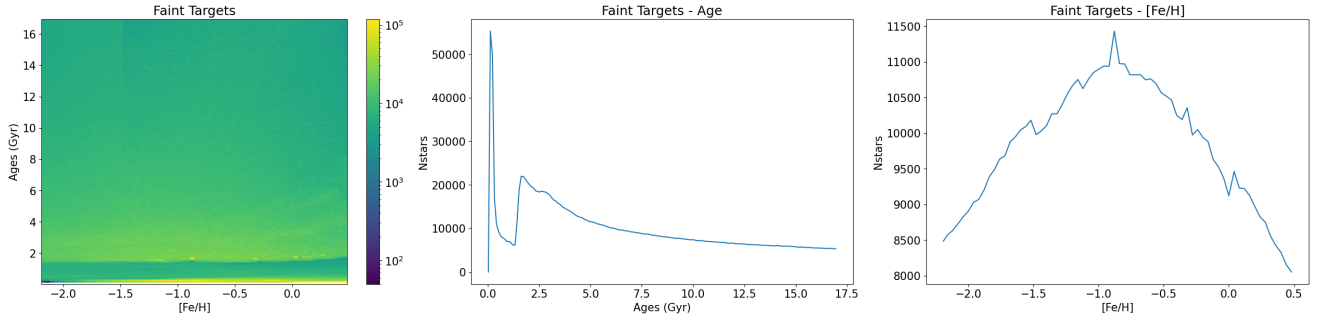


Figure 15. (Left) Number of stars in the target selection box for a stellar population of $10^8 M_{\odot}$, as a function of age and metallicity. There are regions of parameter space (e.g., old, metal-poor), where no stars are expected to be observed. (Middle). Number of stars in the target selection box for a stellar population of $10^8 M_{\odot}$, averaged over metallicity and showing the age dependence. There is a sharp peak around 0.15 Gyr, and a “valley” at 0.3–1.5 Gyr. (Right) The same, but averaged over age and showing the metallicity dependence.

zero. We convert our distribution of number of stars into a probability by simply normalized $N_{\text{stars}}([\text{Fe}/\text{H}], \text{Age})$

$$P_{\text{stars}}([\text{Fe}/\text{H}], \text{Age}) = \frac{N_{\text{stars}}([\text{Fe}/\text{H}], \text{Age})}{\sum N_{\text{stars}}([\text{Fe}/\text{H}], \text{Age})} \quad (18)$$

We use this information to produce a “joint” PDF by taking the product of the two PDFs.

$$P_{\text{joint}}([\text{Fe}/\text{H}], \text{Age}) = P_{\text{meas}}([\text{Fe}/\text{H}], \text{Age}) \times P_{\text{stars}}([\text{Fe}/\text{H}], \text{Age}) \quad (19)$$

The final M_{SP} value for a given APOGEE star is then calculated by taking a weighted mean of $M_{\text{SP}}([\text{Fe}/\text{H}], \text{Age})$ with the joint PDF. Since the faint limit of the FntRGB target selection box varies from field to field, we calculated the number of stars in the FntRGB box for 0.1 mag intervals from 12.8 to 15.3. Finally, the M_{SP} value is multiplied by the “selection function” (from the first step) to calculate the final selection function-corrected “stellar population mass” $M_{\text{SP},\text{SF}}$ value for one of our stars. This is the value that is used for “weighting” in many of the following calculations.

10 RESULTS

10.1 The LMC Extinction Map

The G band extinction map for the LMC can be seen in Figure 16. Interestingly there appears to be a band in the northern part of the LMC with low extinction for radii between ~ 2 kpc and ~ 6 kpc. This contrasts the southern part and center of the galaxy especially for the western side which is closest to the Small Magellanic Cloud (SMC).

10.2 The LMC Age Map, Age-Radius Relation, & Age Distribution

The 2-D median age map of the LMC shows that the center of the galaxy tends to be slightly younger than the outskirts with a wide range of values for the age dispersion (see Figure 17). A clear trend is evident in the age uncertainties, where older ages typically have larger uncertainties. The age uncertainties are calculated using standard error propagation techniques and interpolated splines. The uncertainties shown in the left panel of the age map. It is obvious that these uncertainties suggest great accuracy in the ages. When validating ages, Figure 13 shows that most stars fall within 10% of the 1-to-1 line reinforcing the accuracy in the LMC ages. But regardless the derived uncertainties for the LMC ages should be considered lower limits as they are statistical uncertainties and other systematic

sources of uncertainties could contribute. Some uncertainties of the LMC stars appear to be very close to 0 Gyr. For these stars it is probably best to impose a minimum uncertainty of $\sim 2.5\%$. This estimation is based on clear envelop that can be seen in the left panel of Figure 17.

To gain another perspective on the spatial distribution of stars, we look at the age-radius relation for the median age for each field. Fitting a quartic function to the median field ages gives:

$$\text{age} = -0.03159r^4 + 0.4015r^3 - 1.443r^2 + 1.603r + 5.452 \quad (20)$$

where r is the elliptical radius given by Equation 4. Quartic functions were chosen as visually the field points and the trends matched best without going to a higher order. A plot of the age-radius relations can be seen in Figure 18. In the left panel, the nonlinearity is clearly evident.

The age map suggests that young ages are widespread, but more centrally located. The top panel of Figure 19 shows the age distribution of individual stars and indicates that there are substantially more young stars, though this could be misleading. Using the bias correction and stellar population mass calculation from Section 9 shows that the corrected-age distribution is somewhat different (see the bottom panel of Figure 19). The first noticeable feature of the corrected distribution is the recent increase in stellar population mass (or star formation rate) consistent with many of the other results. Second, there is a wide peak or plateau for ages ~ 3 Gyr to ~ 7 Gyr.

10.3 The LMC Age-Metallicity Relation

In Figure 20, the age-metallicity relation (AMR) is fairly flat between 5 and 15 Gyr. Anything younger than 5 Gyr tends to show increasing metallicity with a rapid increase for stars with ages $\lesssim 2$ Gyr, most likely related to the close interaction between the Clouds mentioned before. When comparing the AMR to LMC clusters from Harris & Zaritsky (2009) (hereafter, HZ09), we find that the younger clusters tend to agree better than the older ones. Notably, the older clusters do bunch up at the age of the universe, but do not follow the AMR derived in this work.

10.4 Asymmetric Drift

We briefly investigated the LMC’s kinematics as a function of our derived ages by assuming that all of our stars lie in the LMC disk plane, and applying the disk kinematic and geometric model from

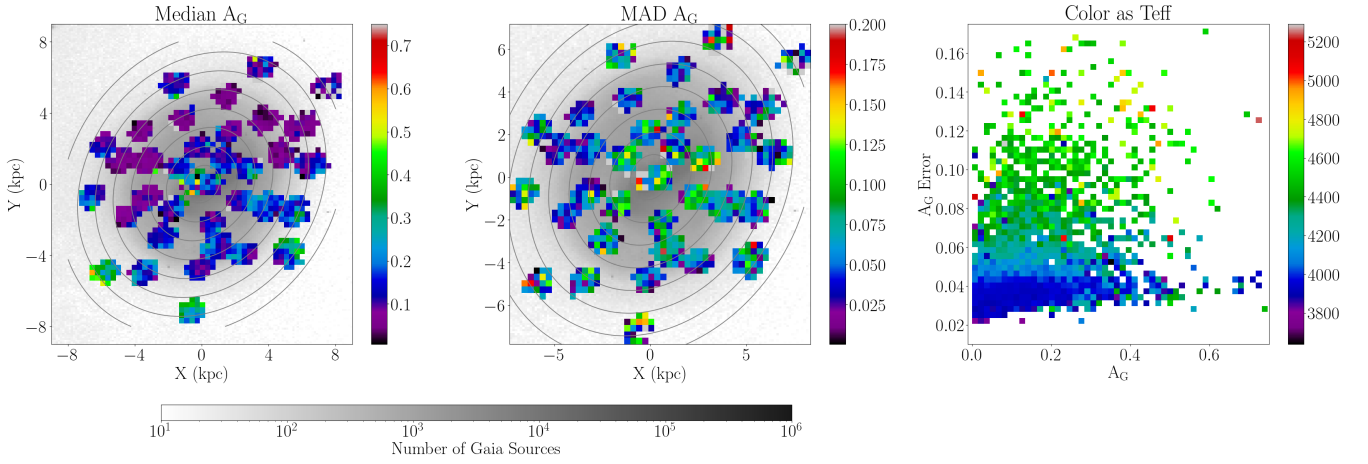


Figure 16. (Left) The G band extinction map for the LMC with the Gaia source number density in the background. In the map there is clearly a band of low extinction between ~ 2 to ~ 6 kpc in the north. (Center) The dispersion in extinction for each of the bins using MAD also with the Gaia background. (Right) The extinction errors as a function of the extinction colored by the T_{eff} of each star. There is a definite correlation between the T_{eff} of a star and calculate extinction error probably due to the steepness in the color–teff relations.

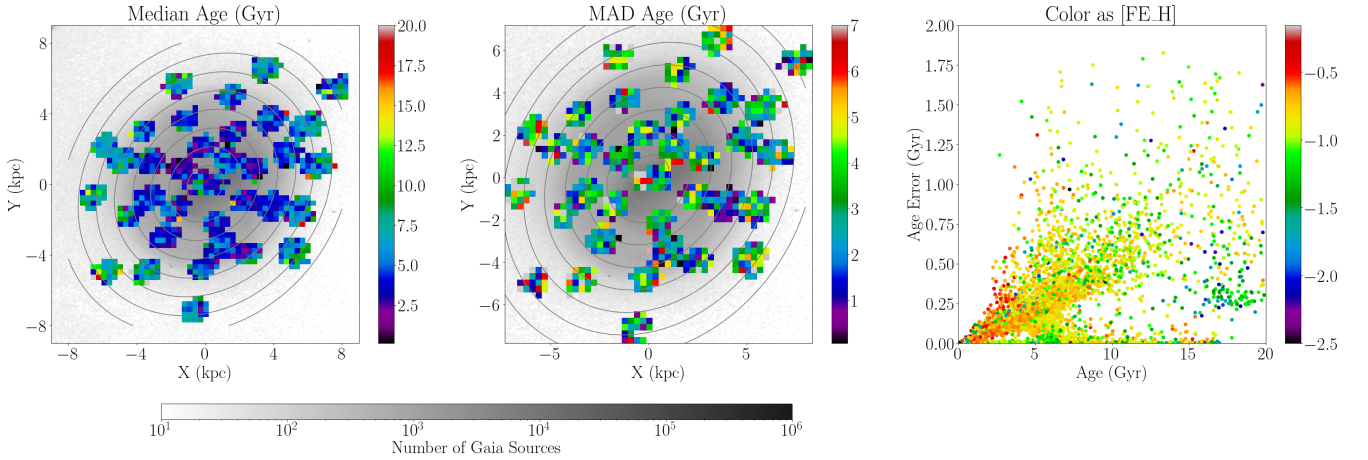


Figure 17. (Left) The age map for the LMC with the Gaia source number density in the background. (Center) The dispersion in age for each of the bins using MAD also with the Gaia background. (Right) The age errors as a function of the age colored by the [Fe/H] of each star. Most derived LMC have uncertainties that are $<10\%$ suggesting great accuracy. There is a band of stars with uncertainties that appear to approach zero, but based on the visible envelop, the best course of action is to inflate any errors for these stars to at least 2.5% .

Choi et al. (2022) to derive the velocity components v_ϕ , v_r , v_z , and their associated errors, from our measured proper motions and line-of-sight velocities. Figure 21 shows the mean values of the velocity components and their dispersions as a function of age, where we have restricted the sample to include only those stars with age < 15 Gyr, velocity errors $< 15 \text{ km s}^{-1}$ in v_ϕ and v_r , errors $< 7.5 \text{ km s}^{-1}$ in v_z , and in-plane radius $R > 3$ kpc; the limit on the radius is to ensure that we sample only the flat portion of the rotation curve.

As seen in the figure, the mean v_z is close to 0 at all ages, while its associated dispersion rises from $< 20 \text{ km s}^{-1}$ at the youngest ages to nearly 30 km s^{-1} at 10 Gyr and beyond. This is expected behavior for a population that is dynamically heated over time. The mean v_r is also small at all ages, but slowly increasing with larger age to a value of $\sim 8 \text{ km s}^{-1}$ beyond 10 Gyr. The dispersion in v_r also grows with age, from $\sim 25 \text{ km s}^{-1}$ at 2.5 Gyr to $\sim 35 \text{ km s}^{-1}$ at 10 Gyr. As we also see some correlation between v_r and azimuthal angle, the small but positive v_r may be a sign that the disk inclination changes in the periphery, where older stars predominate. Finally, the mean

v_ϕ clearly decreases with age, from a peak of $\sim 80 \text{ km s}^{-1}$ at 2.5 Gyr to a minimum of $\sim 60 \text{ km s}^{-1}$ at 10 Gyr, with roughly constant dispersion at all ages. The significant decrease in mean v_ϕ is evidence for asymmetric drift, in which stars which started on nearly circular orbits acquire random deflections over time, which when combined with a decreasing density distribution as a function of radius leads to a suppression of the maximum observed rotational velocity. We can use this observation of asymmetric drift to estimate the circular velocity of the LMC out to the radius limit of our sample. As shown in Binney & Tremaine (1987), we expect the magnitude of the asymmetric drift, $v_c - \overline{v_\phi}$ to be proportional to the radial velocity dispersion σ_r^2 , as the effect of asymmetric drift comes from the preferential selection of stars on the slower portions of their elliptical orbits at any given radius. Thus if we can measure asymmetric drift at two different epochs t_1 and t_2 , and assume that the density distribution is the same

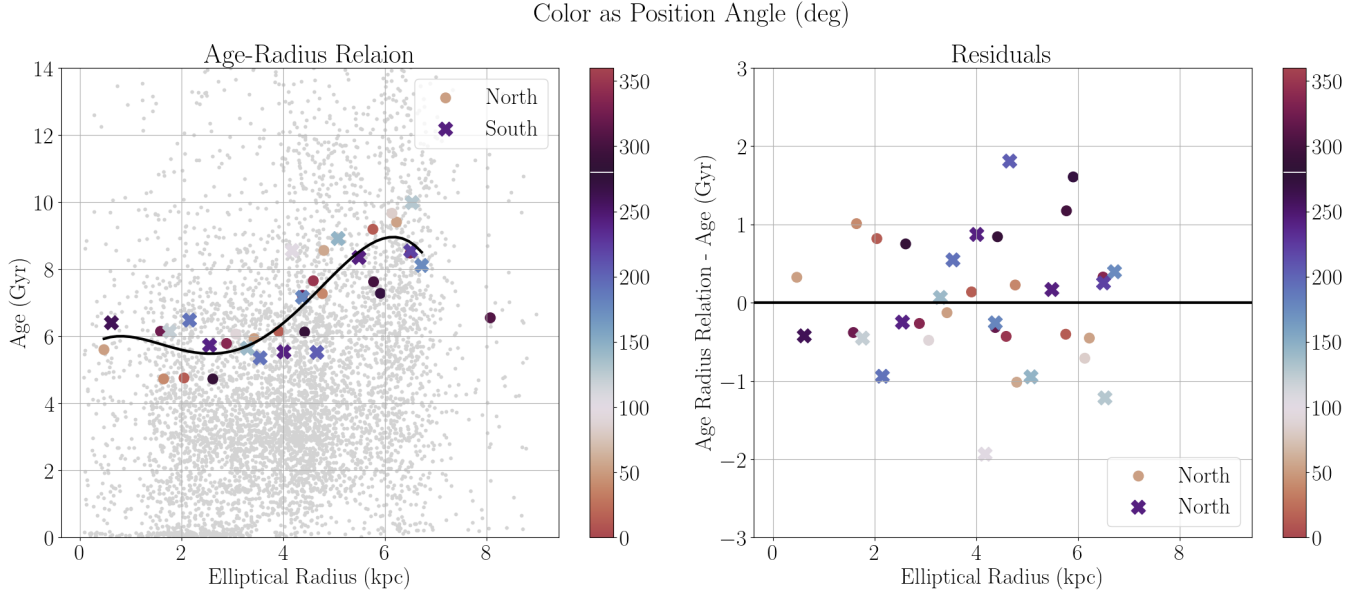


Figure 18. (Left) The age-radius relation for the LMC represented with the black solid line (see Equation 20). Individual LMC stars are shown in the background as light grey dots. The median ages for each of the LMC fields are overplotted as dots and xs colored in function of position angles. Northern fields are represented by dots while southern fields are represented by xs. It is clear that for inner radii that the northern fields are slightly younger than the southern fields at corresponding radii. (Right) The residuals of the quartic function fit. The MAD of the residuals is -0.19 for the clusters compared to 2.17 for the individual stars.

for stars with those ages, we can solve for the circular velocity v_c :

$$v_c = \frac{v_{\phi,1} - v_{\phi,2} \sigma_{r,1}^2 / \sigma_{r,2}^2}{1 - \sigma_{r,1}^2 / \sigma_{r,2}^2} \quad (21)$$

where $v_{\phi,1}$, $v_{\phi,2}$, $\sigma_{r,1}$, and $\sigma_{r,2}$ refer to the mean rotational velocity and radial velocity dispersion at epochs 1 and 2. Taking $v_{\phi,1} = 80 \text{ km s}^{-1}$, $v_{\phi,2} = 60 \text{ km s}^{-1}$, $\sigma_{r,1} = 25 \text{ km s}^{-1}$, and $\sigma_{r,2} = 35 \text{ km s}^{-1}$, we find $v_c \sim 100 \text{ km s}^{-1}$. As the outermost in-plane radius of our sample is 10 kpc, we can then conclude that the mass of the LMC enclosed within 10 kpc is $2.3 \times 10^{10} M_{\odot}$. If the rotation curve remains flat out to 15 kpc, as concluded by Besla (2015), then the total mass of the LMC is at least $3.5 \times 10^{10} M_{\odot}$, in good agreement with the value determined therein.

11 DISCUSSION

The extinction of the LMC has been recently explored with the SMASH data (Choi et al. 2018a). In that paper, the extinction map was derived using red clump stars. This map was chosen to compare to because it is recent and has high resolution coverage of the LMC. In addition, the Choi et al. (2018a) map agrees well with the average reddening value for the LMC found by Zaritsky et al. (2004); Haschke et al. (2011); Bell et al. (2022) and also with the Schlegel et al. (1998) map. In order to compare the derived reddening and the extinction calculated in this work, CCM89 is used to convert the SMASH values to A_G . In Figure 22, the left and right panels show the extinctions from this work and the SMASH $E(g-i)$ converted to A_G , respectively. The right panel of the same figure shows the residuals which reveal a median offset of 0.093 mag while with the APOKASC validation there appears to be an offset of 0.043 mag suggesting that the method in this work slightly underestimates extinction compared to previous literature results. It is not entirely clear what the cause of this could be.

The discrepancies in the extinction values may come from the spread of isochrone points in the isochrone photometry- T_{eff} relations. The extinction method only fits to the locus of the isochrone points and the method in section 7.1 essentially uses a weighted average of the across all bands, which may compound the width effect.

The age map for the LMC shows a large concentration of younger stars in the center of the galaxy with mean age increasing towards the outskirts. Many of the central young stars are thought to have been created as the result of an interaction between the LMC and SMC as the LMC experienced a burst of star formation at that time (Nidever et al. 2020). This is one of the first times the spatial distribution of ages in the LMC has been done and so there are not many literature sources available to compare with.

The age-radius relation is consistent with this result showing a positive gradient (see the left panel of Figure 18). The age-radius relation is clearly not flat for the LMC nor is it simply linear, but there is a distinct increase in the median age of stars with larger radii similar to what is seen in the age map. This shows that earlier in its history the LMC experienced more widespread star formation even out to its furthest limits, while at more recent times star formation has been concentrated toward the center, as previously mentioned. This change in behavior could be due to the outer LMC gas being stripped off by the interaction of the LMC with the SMC or from the ram pressure in the Milky Way's hot halo. Another mechanism that can affect the distribution of stars in a galaxy is radial migration (e.g. Sellwood & Binney 2002; Sellwood 2014). Radial migration leads to changes in the metallicity gradient of a galaxy and because metallicity is a proxy for age, this should also affect the age-radius relation.

In the left of Figure 18, the majority of the northern fields are below the trendline for radii $< 4 \text{ kpc}$, but the southern fields tend to be above it producing a north-south dichotomy. There is a single spiral arm structure present in the inner northern fields with approximately

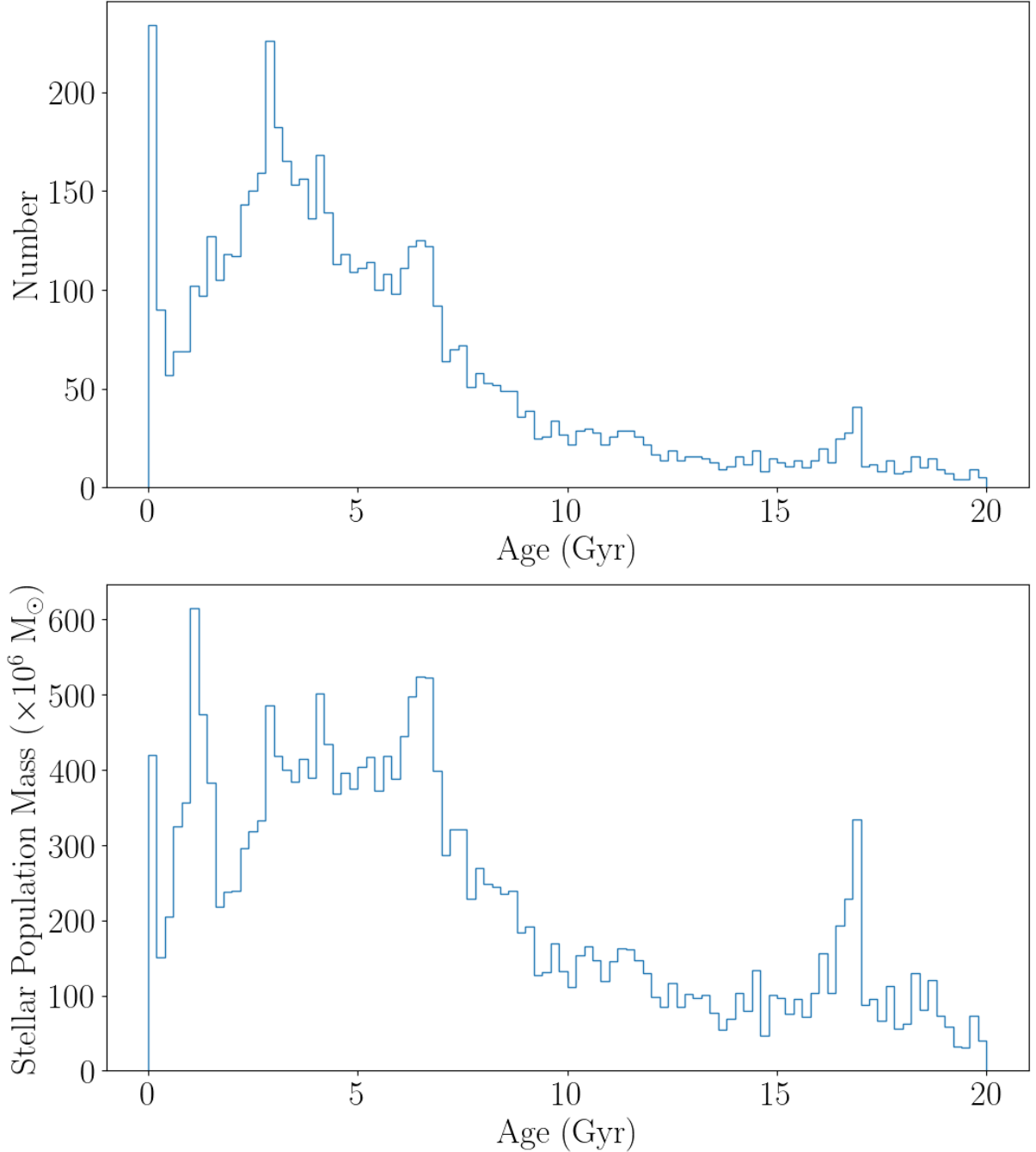


Figure 19. (*Top*) A histogram of the ages calculated for the individual stars in the sample. The peak at 0 Gyr is made mostly of blue loop stars with some potentially bad results where stars could be assigned younger ages than they should be. The peaks less than 10 Gyr may suggest different star forming events while the peak at ~ 17 corresponds to the age of the oldest isochrone. (*Bottom*) A histogram showing the stellar population mass corresponding to the calculated ages corrected for the bias according to section 9. The first two peaks in the plateau between ~ 2.5 – 5.0 Gyr do not appear to be temporally separated, but the third peak is. The supposed separation between the first two peaks may be an unphysical artefact.

the right age to be created through a known interaction between the LMC and SMC ~ 2 Gyr ago. Through N-body simulations it has been shown that single spiral arms can be created through intergalactic tidal interactions (e.g. Berentzen et al. 2003; Pearson et al. 2018). This suggests that the spiral arm in the north was likely created by this major event.

The AMR of the LMC is mostly flat, increasing very slowly over time. In the upper panel of Figure 20 there is a clear recent increase

in $[\text{Fe}/\text{H}]$ coincident with the LMC-SMC interaction. The derived AMR shows decent agreement for the LMC globular clusters from HZ09, except close to the age of the universe. This is also true of AMRs derived using clusters such as in Olszewski et al. (1991), Dirsch et al. (2000), and Grocholski et al. (2006), which all exhibit the downturn near the age of the universe while the one derived in this work does not. The LMC AMR derived from individual RGB stars in Carrera et al. (2008) matches even better than the cluster AMRs,

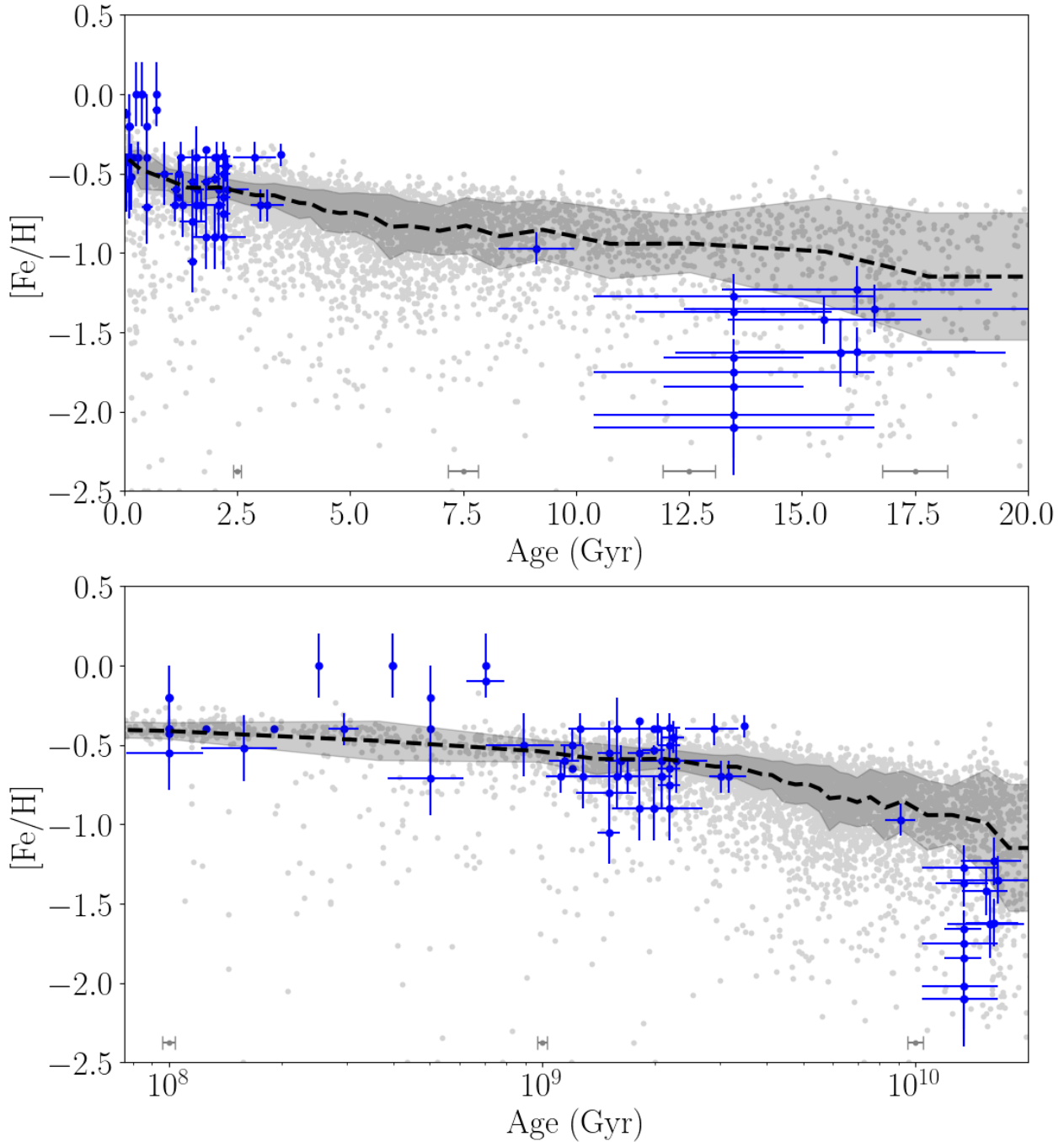


Figure 20. (Top) The AMR of the LMC calculated with the individual stars shown as the black dashed line. The APOGEE stars themselves are grey. The grey region shows the 1σ limit around the AMR. The blue points with error bars represent the 85 LMC clusters from HZ09. The grey points at the bottom show the characteristic error in the grey points. Clearly the largest disagreement with clusters happens for the oldest ages where measurements get dominated by noise. (Bottom) The same as the top, but with a log scale which highlights younger ages.

but the downturn is still seen. It appears that for field star derived AMRs, the metallicities for intermediate ages tends to be slightly higher than what is seen according to clusters. This could be due to a known lack of clusters for those ages Rich et al. (2001), Bekki et al. (2004), and Mackey et al. (2006). For the oldest ages, both the cluster and field star derived AMRs do show a downturn around the age of the universe that is not present in the AMR derived here. A possible reason for this is that the stars with ages >12.5 Gyr are dominated by measurement uncertainties in their parameters that get

propagated through the age method. Other sources of this effect could be systematics with the PARSEC models or the interpolation favors pushing metal poor stars to older ages.

Previously the difference in the AMR for the LMC disk and bar have been investigated in (Cole et al. 2005; Carrera et al. 2008, 2011). Selecting the APOGEE bar stars in this work, it was found that there is an increase in $[\text{Fe}/\text{H}]$ in the last ~ 1 Gyr for the both the bar and the LMC disk. This contradicts Cole et al. (2005) and Carrera et al. (2008), which found that there is not an appreciable

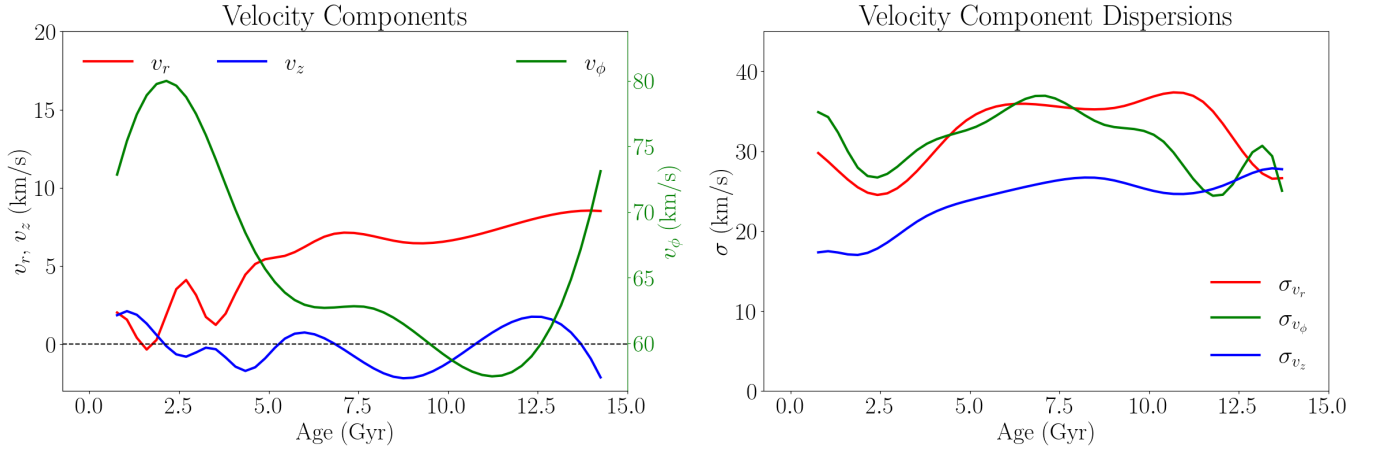


Figure 21. (Left) The different components of the velocity as functions of age. The v_r and v_z are shown in red and blue respectively. These two velocity components use the black axis on the left. The 0.0 km/s for this is included as a dashed line. Both v_r and v_ϕ components stay close to zero. The v_r curve shows that there is an increase starting around ages of 5 Gyr, though for even the oldest ages this component does not get above 10 km/s. The v_ϕ velocity is shown as a green curve and uses the green axis on the right. For ages ≤ 2.5 Gyr there is a large increase in v_ϕ and then from 2.5–5.0 Gyr there is a decrease down to about ~ 67 km/s and then an increase for the oldest stars. (Right) The different components of the velocity dispersion as functions of age.

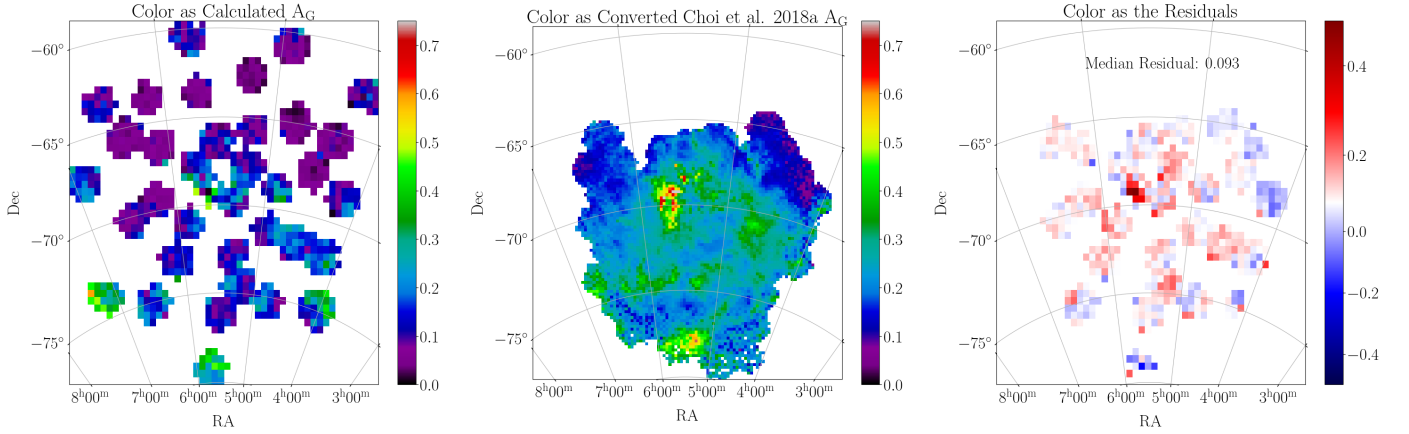


Figure 22. (Left) The G band extinction map for the LMC. This is the same map as seen in Figure 16. (Center) The extinction map of LMC using A_G derived from Choi et al. (2018a) and the CCM89 extinction law. (Right) The residuals between the converted Choi et al. (2018a) A_G and the calculated A_G from this work with a median residual of 0.093 mag suggesting a slight offset.

increase in $[\text{Fe}/\text{H}]$ for the bar in the last Gyr or so. Though there are less stars in the bar for older ages, the AMR for the bar is largely flat for ages older than 5 Gyr. For the most part the bar AMR suggests that these stars are more metal-rich for all times.

The detection of asymmetric drift in the stellar kinematics as a function of age is expected, and thus lends support to our ability to measure ages with our method. We used the measured evolution in asymmetric drift to estimate the LMC’s circular velocity and thus its total mass out to 10 kpc; our estimate of $2.3 \times 10^{10} M_\odot$ within 10 kpc is $\sim 10\%$ higher than e.g. van der Marel & Kallivayalil (2014), but in overall good agreement.

12 SUMMARY

We present an isochrone based method to calculate the ages of individual RGB stars and use this to find the ages of more than 6000 stars in the LMC. This method makes use of both photometry and

spectroscopy and requires the distance to be known. The “A codeTe stellAr ageS” (Aetas) code used throughout this work is available online⁸. In addition the age method can be easily adapted to find the age of any individual star under some minimal constraints. Aetas requires that the photometry, distance, $[\text{Fe}/\text{H}]$, $[\alpha/\text{Fe}]$, T_{eff} , and $\log g$ be already measured. In order to use a different set of isochrones with Aetas, the appropriate labels will need to be changed to match the input table.

- We have used accurate photometry, spectroscopy and isochrones to determine ages statistically accurate to $\sim 1\text{--}2\%$ and systematically accurate to $\sim 1\text{--}3$ Gyr of stars in the LMC disk.
- Our method determined age and extinction simultaneously. Our LMC extinction map corresponds well with other literature extinction maps (e.g., Choi et al. 2018a).

⁸ <https://github.com/JoshuaPovick/aetas>

- The median age is relatively flat with radius at ~ 4 Gyr out to ~ 4 kpc. Then it rises to ~ 6 Gyr until the edge of our coverage at 7 kpc.
- We see an Age dichotomy in the LMC disk, with northern fields slightly younger than same ones at the same elliptical radius.
- Exploring the relation between the derived ages and kinematics of the LMC shows evidence of asymmetric drift.

Papers II and III in this series will use the ages determined in this work and study the chemical age-radius trends in both the LMC and SMC.

ACKNOWLEDGEMENTS

J.T.P. acknowledges support for this research from the National Science Foundation (AST-1908331) and the Montana Space Grant Consortium Graduate Fellowship. D.L.N. acknowledges support for this research from the National Science Foundation (AST-1908331)

Funding for the Sloan Digital Sky Survey IV has been provided by the Alfred P. Sloan Foundation, the U.S. Department of Energy Office of Science, and the Participating Institutions.

SDSS-IV acknowledges support and resources from the Center for High Performance Computing at the University of Utah. The SDSS website is www.sdss.org.

SDSS-IV is managed by the Astrophysical Research Consortium for the Participating Institutions of the SDSS Collaboration including the Brazilian Participation Group, the Carnegie Institution for Science, Carnegie Mellon University, Center for Astrophysics | Harvard & Smithsonian, the Chilean Participation Group, the French Participation Group, Instituto de Astrofísica de Canarias, The Johns Hopkins University, Kavli Institute for the Physics and Mathematics of the Universe (IPMU) / University of Tokyo, the Korean Participation Group, Lawrence Berkeley National Laboratory, Leibniz Institut für Astrophysik Potsdam (AIP), Max-Planck-Institut für Astronomie (MPIA Heidelberg), Max-Planck-Institut für Astrophysik (MPA Garching), Max-Planck-Institut für Extraterrestrische Physik (MPE), National Astronomical Observatories of China, New Mexico State University, New York University, University of Notre Dame, Observatório Nacional / MCTI, The Ohio State University, Pennsylvania State University, Shanghai Astronomical Observatory, United Kingdom Participation Group, Universidad Nacional Autónoma de México, University of Arizona, University of Colorado Boulder, University of Oxford, University of Portsmouth, University of Utah, University of Virginia, University of Washington, University of Wisconsin, Vanderbilt University, and Yale University.

This work has made use of data from the European Space Agency (ESA) mission *Gaia* (<https://www.cosmos.esa.int/gaia>), processed by the *Gaia* Data Processing and Analysis Consortium (DPAC, <https://www.cosmos.esa.int/web/gaia/dpac/consortium>). Funding for the DPAC has been provided by national institutions, in particular the institutions participating in the *Gaia* Multilateral Agreement.

Software: Astropy (Astropy Collaboration et al. 2018, 2013), Matplotlib (Hunter 2007), NumPy (Harris et al. 2020), SciPy (Virtanen et al. 2020)

DATA AVAILABILITY

All APOGEE DR17 data used in this study is publicly available and can be found at: https://www.sdss4.org/dr17/data_access/. This dataset does include the corresponding *Gaia* and 2MASS data in addition to the spectroscopic data.

REFERENCES

- Abdurro'uf et al., 2022, *ApJS*, **259**, 35
- Ahumada R., et al., 2020, *ApJS*, **249**, 3
- Allende Prieto C., Beers T. C., Wilhelm R., Newberg H. J., Rockosi C. M., Yanny B., Lee Y. S., 2006, *ApJ*, **636**, 804
- Asplund M., Amarsi A. M., Grevesse N., 2021, *A&A*, **653**, A141
- Astropy Collaboration et al., 2013, *A&A*, **558**, A33
- Astropy Collaboration et al., 2018, *AJ*, **156**, 123
- Barnes S. A., 2007, *ApJ*, **669**, 1167
- Bekki K., Couch W. J., Beasley M. A., Forbes D. A., Chiba M., Da Costa G. S., 2004, *ApJ*, **610**, L93
- Bell C. P. M., et al., 2022, *MNRAS*, **516**, 824
- Berentzen I., Athanassoula E., Heller C. H., Fricke K. J., 2003, *MNRAS*, **341**, 343
- Besla G., 2015, The Orbits and Total Mass of the Magellanic Clouds ([arXiv:1511.03346](https://arxiv.org/abs/1511.03346))
- Binney J., Tremaine S., 1987, Galactic dynamics. Princeton university press
- Blanton M. R., et al., 2017, *AJ*, **154**, 28
- Bowen I., Vaughan A., 1973, *Appl. Opt.*, **12**, 1430
- Bressan A., Marigo P., Girardi L., Salasnich B., Dal Cero C., Rubele S., Nanni A., 2012, *MNRAS*, **427**, 127
- Cardelli J. A., Clayton G. C., Mathis J. S., 1989, *ApJ*, **345**, 245
- Carrera R., Gallart C., Hardy E., Aparicio A., Zinn R., 2008, *AJ*, **135**, 836
- Carrera R., Gallart C., Aparicio A., Hardy E., 2011, *The Astronomical Journal*, **142**, 61
- Choi Y., et al., 2018a, *ApJ*, **866**, 90
- Choi Y., et al., 2018b, *ApJ*, **869**, 125
- Choi Y., Olsen K. A. G., Besla G., van der Marel R. P., Zivick P., Kallivayalil N., Nidever D. L., 2022, *ApJ*, **927**, 153
- Choudhury S., et al., 2021, *MNRAS*, **507**, 4752
- Cioni M. R. L., et al., 2011, *A&A*, **527**, A116
- Cole A. A., Tolstoy E., Gallagher John S. I., Smecker-Hane T. A., 2005, *AJ*, **129**, 1465
- Cunha M. S., et al., 2007, *The A&A Review*, **14**, 217
- Da Costa G. S., 1991, in Haynes R., Milne D., eds, *IAU Symposium Vol. 148, The Magellanic Clouds*. p. 183
- Dalcanton J. J., et al., 2012, *ApJS*, **200**, 18
- De Grijs R., Wicker J. E., Bono G., 2014, *AJ*, **147**, 122
- Dirsch B., Richtler T., Gieren W., Hilker M., 2000, *arXiv preprint astro-ph/0004009*
- Feuillet D. K., Bovy J., Holtzman J., Girardi L., MacDonald N., Majewski S. R., Nidever D. L., 2016, *ApJ*, **817**, 40
- Fitzpatrick E. L., 1999, *PASP*, **111**, 63
- Flower P., Geisler D., Hodge P., Olszewski E., Schommer R., 1983, *ApJ*, **275**, 15
- Frebel A., Christlieb N., Norris J. E., Thom C., Beers T. C., Rhee J., 2007, *ApJ*, **660**, L117
- Gaia Collaboration et al., 2016, *A&A*, **595**, A1
- Gaia Collaboration et al., 2021, *A&A*, **649**, A1
- Gaia Collaboration et al., 2022, *arXiv e-prints*, p. [arXiv:2208.00211](https://arxiv.org/abs/2208.00211)
- García-Pérez A. E., et al., 2016, *AJ*, **151**, 144
- Gatto M., et al., 2020, *MNRAS*, **499**, 4114
- Geisler D., Bica E., Dottori H., Claria J. J., Piatti A. E., Santos Joao F. C. J., 1997, *AJ*, **114**, 1920
- Gordon K. D., et al., 2016, *ApJ*, **826**, 104
- Grocholski A. J., Cole A. A., Sarajedini A., Geisler D., Smith V. V., 2006, *AJ*, **132**, 1630
- Gunn J. E., et al., 2006, *AJ*, **131**, 2332
- Harris J., Zaritsky D., 2009, *AJ*, **138**, 1243
- Harris C. R., et al., 2020, *Nature*, **585**, 357
- Haschke R., Grebel E. K., Duffau S., 2011, *AJ*, **141**, 158
- Hill V., et al., 2002, *A&A*, **387**, 560
- Holtzman J. A., Harrison T. E., Coughlin J. L., 2010, *Advances in Astronomy*, **2010**, 193086
- Hubeny I., Allende Prieto C., Osorio Y., Lanz T., 2021, *arXiv e-prints*, p. [arXiv:2104.02829](https://arxiv.org/abs/2104.02829)
- Hunter J. D., 2007, *Computing in Science & Engineering*, **9**, 90

- Jönsson H., et al., 2020, arXiv e-prints, [p. arXiv:2007.05537](https://arxiv.org/abs/2007.05537)
- Kroupa P., 2001, *MNRAS*, 322, 231
- Kroupa P., 2002, *Science*, 295, 82
- Mackey A., Payne M., Gilmore G., 2006, *MNRAS*, 369, 921
- Majewski S. R., et al., 2017, *AJ*, 154, 94
- Mamajek E. E., Hillenbrand L. A., 2008, *ApJ*, 687, 1264
- Marigo P., et al., 2017, *ApJ*, 835, 77
- Mateo M., Hodge P., Schommer R., 1986, *Astrophysical Journal*, Part 1 (ISSN 0004-637X), 311, 113
- Mazzi A., et al., 2021, *MNRAS*, 508, 245
- Meschin I., Gallart C., Aparicio A., Hidalgo S. L., Monelli M., Stetson P. B., Carrera R., 2014, *MNRAS*, 438, 1067
- Monteagudo L., Gallart C., Monelli M., Bernard E. J., Stetson P. B., 2018, *MNRAS*, 473, L16
- Ness M., Hogg D. W., Rix H. W., Martig M., Pinsonneault M. H., Ho A. Y. Q., 2016, *ApJ*, 823, 114
- Nidever D., 2021, dnidever/doppler: Cannon and Payne models, Zenodo, [doi:10.5281/zenodo.4906681](https://doi.org/10.5281/zenodo.4906681)
- Nidever D. L., Majewski S. R., Burton W. B., 2008, *ApJ*, 679, 432
- Nidever D. L., et al., 2015, *AJ*, 150, 173
- Nidever D. L., et al., 2017, *AJ*, 154, 199
- Nidever D. L., et al., 2020, *ApJ*, 895, 88
- Nidever D. L., et al., 2021, *AJ*, 161, 74
- Olszewski E. W., Schommer R. A., Suntzeff N. B., Harris H. C., 1991, *AJ*, 101, 515
- Pearson S., et al., 2018, *MNRAS*, 480, 3069
- Piatti A. E., 2022, *MNRAS*: Letters, 511, L72
- Pinsonneault M., Kawaler S. D., Sofia S., Demarque P., 1989, *The Astrophysical Journal*, 338, 424
- Pinsonneault M. H., et al., 2014, *ApJS*, 215, 19
- Pinsonneault M. H., et al., 2018, *ApJS*, 239, 32
- Rich R. M., Shara M. M., Zurek D., 2001, *AJ*, 122, 842
- Riello M., et al., 2021, *A&A*, 649, A3
- Ripepi V., et al., 2014, *MNRAS*, 442, 1897
- Ruiz-Lara T., et al., 2020, *A&A*, 639, L3
- Salaris M., Chieffi A., Straniero O., 1993, *ApJ*, 414, 580
- Sandage A., 1970, *ApJ*, 162, 841
- Sarajedini A., 2008, *Proceedings of the International Astronomical Union*, 4, 221
- Schlafly E. F., Finkbeiner D. P., Schlegel D. J., Jurić M., Ivezić Ž., Gibson R. R., Knapp G. R., Weaver B. A., 2010, *ApJ*, 725, 1175
- Schlegel D. J., Finkbeiner D. P., Davis M., 1998, *ApJ*, 500, 525
- Sellwood J., 2014, *RvMP*, 86, 1
- Sellwood J. A., Binney J., 2002, *MNRAS*, 336, 785
- Serenelli A., et al., 2017, *The Astrophysical Journal Supplement Series*, 233, 23
- Van Saders J. L., Pinsonneault M. H., 2012, *The Astrophysical Journal*, 746, 16
- Virtanen P., et al., 2020, *Nature Methods*, 17, 261
- Weiss A., Schlattl H., 2008, *Astrophysics and Space Science*, 316, 99
- Weisz D. R., Dolphin A. E., Skillman E. D., Holtzman J., Dalcanton J. J., Cole A. A., Neary K., 2013, *MNRAS*, 431, 364
- Wilson J. C., et al., 2019, *PASP*, 131, 055001
- Zaritsky D., Harris J., Thompson I., 1997, *AJ*, 114, 1002
- Zaritsky D., Harris J., Thompson I. B., Grebel E. K., 2004, *AJ*, 128, 1606
- Zasowski G., et al., 2013, *AJ*, 146, 81
- Zasowski G., et al., 2017, *AJ*, 154, 198
- van der Marel R. P., Cioni M.-R. L., 2001, *AJ*, 122, 1807
- van der Marel R. P., Kallivayalil N., 2014, *ApJ*, 781, 121

APPENDIX A: GAIA DR3 SELECTION

For Figure 1, we use *Gaia* DR3 data to make the background density map, which highlights some of the structures around the Clouds. We use a parallax cut of stars compatible with being more than 20 kpc away at lower than 10% uncertainty. A proper motion cut of a radius of 1.05 mas/yr centered around $(\mu_L, \mu_B) = (1.767, 0.451)$ in Magellanic Stream coordinates (Nidever et al. 2008). A magnitude cut at $G=19.3$ and a cut around the red giant branch sequence in a colour-magnitude diagram.

This paper has been typeset from a \LaTeX file prepared by the author.